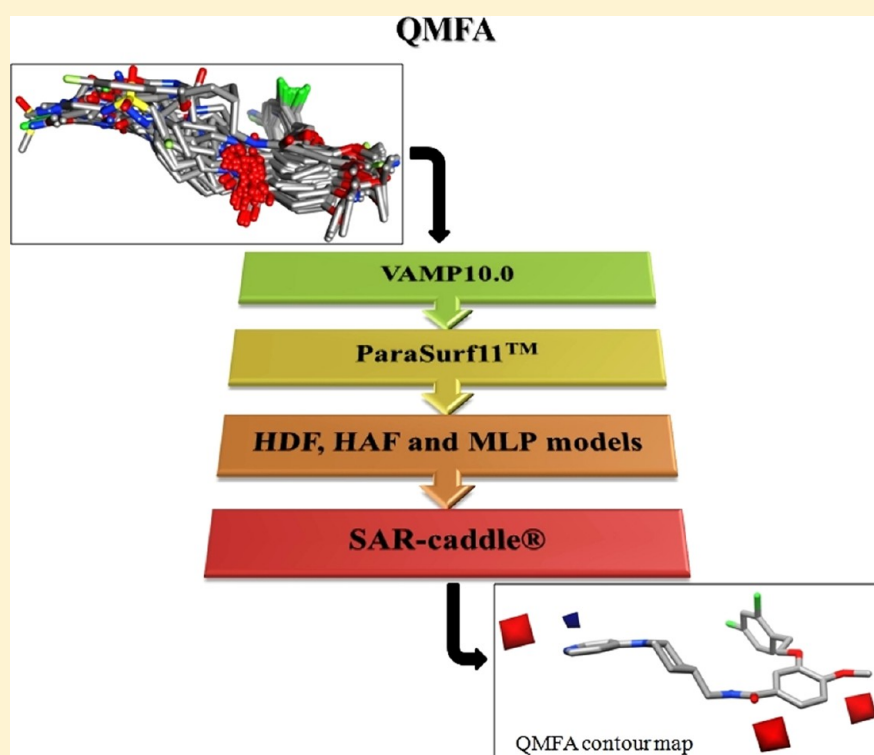


Quantum Mechanics-Based Properties for 3D-QSAR

Ahmed El Kerdawy,[†] Stefan Güssregen,[‡] Hans Matter,[‡] Matthias Hennemann,^{†,§} and Timothy Clark^{*,†,§,||}[†]Computer-Chemie-Centrum, Friedrich-Alexander-Universität Erlangen-Nürnberg, Nögelsbachstraße 25, 91052 Erlangen, Germany[‡]Sanofi-Aventis Deutschland GmbH, R&D, LGCR, Structure, Design and Informatics, 65926 Frankfurt am Main, Germany[§]Interdisciplinary Center for Molecular Materials, Friedrich-Alexander-Universität Erlangen-Nürnberg, Nögelsbachstraße 49, 91052 Erlangen, Germany^{||}Centre for Molecular Design, University of Portsmouth, King Henry Building, Portsmouth PO1 2DY, United Kingdom

S Supporting Information



ABSTRACT: We have used a set of four local properties based on semiempirical molecular orbital calculations (electron density (ρ), hydrogen bond donor field (HDF), hydrogen bond acceptor field (HAF), and molecular lipophilicity potential (MLP)) for 3D-QSAR studies to overcome the limitations of the current force field-based molecular interaction fields (MIFs). These properties can be calculated rapidly and are thus amenable to high-throughput industrial applications. Their statistical performance was compared with that of conventional 3D-QSAR approaches using nine data sets (angiotensin converting enzyme inhibitors (ACE), acetylcholinesterase inhibitors (AChE), benzodiazepine receptor ligands (BZR), cyclooxygenase-2 inhibitors (COX2), dihydrofolate reductase inhibitors (DHFR), glycogen phosphorylase b inhibitors (GPB), thermolysin inhibitors (THER), thrombin inhibitors (THR), and serine protease factor Xa inhibitors (fXa)). The 3D-QSAR models generated were tested thoroughly for robustness and predictive ability. The average performance of the quantum mechanical molecular interaction field (QM-MIF) models for the nine data sets is better than that of the conventional force field-based MIFs. In the individual data sets, the QM-MIF models always perform better than, or as well as, the conventional approaches. It is particularly encouraging that the relative performance of the QM-MIF models improves in the external validation. In addition, the models generated showed statistical stability with respect to model building procedure variations such as grid spacing size and grid orientation. QM-MIF contour maps reproduce the features important for ligand binding for the example data set (factor Xa inhibitors), demonstrating the intuitive chemical interpretability of QM-MIFs.

Received: March 27, 2013

Published: May 21, 2013

■ INTRODUCTION

In drug-design projects, ligand–target interactions form the basis for designing new ligands with improved activity. Medicinal chemists can rely either on knowledge of the biological target (structure-based drug design, SBDD) or of its known ligands (the second binding partner), in ligand-based drug design (LBDD),^{1–3} although the two approaches are often used in parallel.

Currently, the 3D-QSAR techniques comparative molecular field analysis (CoMFA)⁴ and comparative molecular similarity indices analysis (CoMSIA)^{5,6} represent the most successful and widely used LBDD approaches for estimating binding affinity within a specific chemical series of ligands and for guiding the synthesis of new ones.⁷ 3D-QSAR can often give more accurate predicted ligand-binding affinities than SBDD,⁸ although it is limited to the chemical series of ligands on which it was originally trained.

In 3D-QSAR, a statistical analysis, usually partial least-squares (PLS)^{9–11} is carried out to correlate the ligands' molecular structures to their biological endpoint (usually a measure of binding affinity or agonistic effects).^{7,12} In CoMFA, the molecular structure is described by molecular interaction fields (MIFs), which capture molecular interaction characteristics that correlate with the biological activity. The MIFs are generated by computing the interactions of a probe atom or molecule with the aligned ligands' structures at different positions on a 3D-grid. Conventional CoMFA uses electrostatic and steric MIFs, which are calculated using atom-centered monopoles^{6–12} and Lennard–Jones potentials, respectively.⁷ In CoMSIA, similarity indices are used to describe the molecular structure. It includes hydrogen bonding and hydrophobic fields^{6,13–19} in addition to the steric and electrostatic fields. Generally, the quality and accuracy of these fields affect the quality and predictivity of the 3D-QSAR model significantly.

Different MIFs are typically calculated using classical force fields or sometimes generated using a knowledge-based description, as in the case of hydrogen bonding.^{14,15} This means that the known weaknesses associated with the force fields are carried over into the MIFs.

These include the following: (a) They cannot describe important noncovalent interactions such as hydrogen bonding accurately. A recent comprehensive study²⁰ showed that most of the currently available force fields underestimate the stabilization that results from hydrogen bonding. (b) They are unable to describe nonclassical but important noncovalent interactions such as halogen bonding.^{21–23} Because the Coulomb potentials are based on atom-centered point charges, the force field is unable to describe the electron density anisotropy of halogen atoms²⁴ known as the σ -hole.^{25,26} This is an area of positive electrostatic potential collinear with the C-halogen bond axis surrounded by a belt of negative potential orthogonal to it. Very recently, positive pseudo-atoms or point charges on the halogen atom in the position of the σ -hole have been introduced to some force fields (e.g., AMBER and OPLS-AAx) in order to describe this electrostatic anisotropy.^{27–30} (c) Because of their atom-centered charge model, which does not take charge-delocalization into account, classical force fields sometimes also fail to describe important noncovalent interactions such as cation– π ³¹ and π – π stacking³² interactions.³³ (d) Force field transferability is not guaranteed. How accurate is the treatment of a molecule that is not contained in the training set originally used to optimize the force field?²

The increasing use of quantum mechanical (QM) methods in computer-aided drug design (CADD) is not only the result of the ever growing computational power but also due to the more realistic physical model on which QM techniques are based. Across the range from computationally expensive *ab initio* methods via density-functional theory to the fast semiempirical techniques, QM approaches do not suffer from the limitations inherent to the ball-and-spring description and the fixed-charge approximation used in most force fields,^{33–37} although force fields arguably do a better job in treating dispersion than most QM techniques.

Employing QM-based properties in QSAR studies is not new; some previous studies have taken advantage of QM-based MIFs to generate more robust QSAR models than conventional ones.^{24,38–50} Despite this improvement, these QM-based approaches often have significant disadvantages: (a) Most of these approaches use descriptors derived from density-functional theory (DFT) calculations, so they are too computationally demanding to treat data sets with very large numbers of compounds, especially when compared to the conventional 3D-QSAR fields' computational demand. (b) Some of these descriptors were tailored to a specific data set. We cannot assume that descriptors optimized for one data set will work equally well with others. (c) QM descriptors cannot always be interpreted straightforwardly and intuitively, which is a critical feature for 3D-QSAR descriptors intended to guide medicinal chemists in designing new ligands.

We now describe a set of QM-based properties designed to avoid the force field drawbacks mentioned above but still to be fast enough for routine use on very large data sets because they are based on semiempirical molecular-orbital (MO) theory.⁵¹ Despite their solid theoretical foundation, their direct physical meaning allows their intuitive interpretation, which is important for their use as 3D-QSAR MIFs. They will also be tested using several diverse data sets to ensure their generality and their potential use as universal 3D-QSAR MIFs.

QM-Properties. (a). *Electron Density (ρ)*. Electron density describes the probability of finding electrons in a specific position in the space around the molecule.⁵² It can therefore be used in a 3D-QSAR context to describe the steric extent (shape and size) of the molecules.⁵³ It can be considered the quantum mechanical equivalent of the steric field used in conventional 3D-QSAR. Figure 1 shows the electron density of *p*-chlorobenzoic acid as

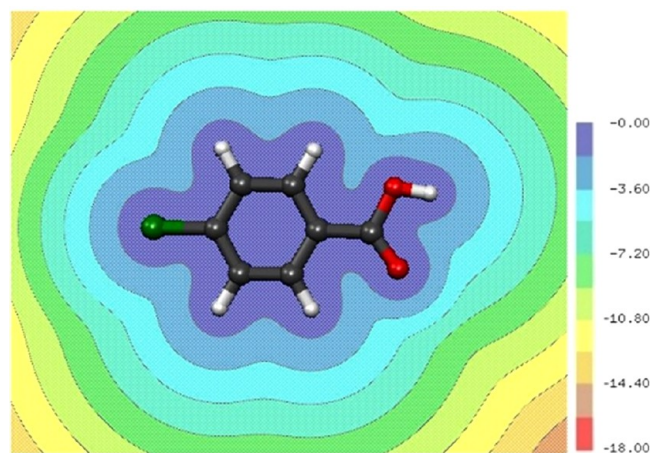


Figure 1. Contour plot showing the base-10 logarithm of the electron density (ρ , $\text{e } \text{\AA}^{-3}$) of *p*-chlorobenzoic acid in the molecular plane and extending 6 Å outside the molecule.

an example to illustrate how it describes the shape and size of the molecule. The electron density value decays gradually with increasing distance from the atomic nuclei, thus describing the steric extent of the molecule. In the current work, the electron density was calculated using the NDDO-based semiempirical MO theory employing the AM1 Hamiltonian.^{54,55} Note that conventional steric fields are based on isotropic Lennard–Jones potentials, so that they cannot treat phenomena such as “polar flattening” of halogens (Figure 2),^{56,57} which are automatically captured by the extent of the electron density.

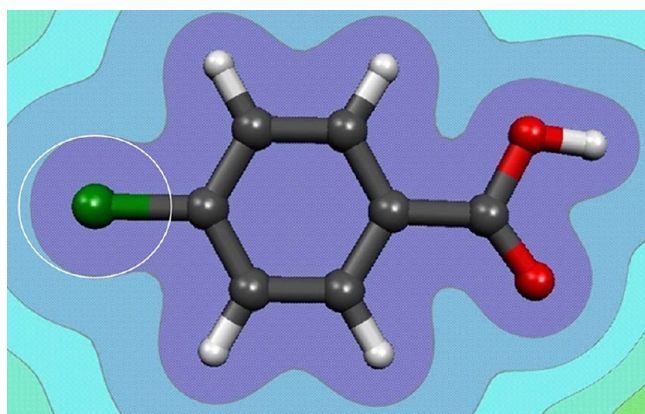


Figure 2. Contour map of the electron density (ρ) of *p*-chlorobenzoic acid describes the “polar flattening” of the halogen atom. The white circle is for guidance and is centered on the chlorine atom.

(b). *Hydrogen Bond Donor Field (HDF)*. On the basis of our previous work,⁵⁸ the HDF is calculated at the grid points around the molecule using feed-forward artificial neural nets (ANN) that were trained to recognize H-bond donor sites around drug-like molecules using the local properties electron density, molecular electrostatic potential,^{59,60} local ionization energy,^{61–64} local electron affinity,^{65,66} local polarizability,^{65,67–70} and their gradients as descriptors. Data were calculated using the AM1 Hamiltonian. The neural nets were trained using calculated DFT (ω B97X-D/aug-cc-pVDZ) interaction energies between a series of model central molecules and H-bond donor or acceptor probes situated on grid points around the central molecule.⁵⁸ Grid points inside the van der Waals volume of the molecule lead to strong repulsions and were therefore set to a high cutoff value ($100 \text{ kcal mol}^{-1}$).²⁴ The probe molecules include water, ammonia, and formamide as both donors and acceptors and OH^- as a charged acceptor. These models are also available and could be used to generate the HDF at the grid points for 3D-QSAR studies. Figure 3 shows the HDF around *p*-chlorobenzoic acid as an example that illustrates the ability of the ANN model to map both classical and nonclassical H-bonding and halogen-bonding donor sites.

(c). *Hydrogen Bond Acceptor Field (HAF)*. HAF is generated analogously to HDF but with an ANN trained using the DFT-calculated interaction energies obtained using H_2O as the H-bond donor probe as the target value.⁵⁸ Grid points inside the van der Waals volume were set to $100 \text{ kcal mol}^{-1}$. In addition to the donor/acceptor molecules described above, NH_4^+ was also used as a charged H-bond donor probe. Figures 4 and 5 show the water-based HAF around *p*-chlorobenzoic acid, which illustrates the ability of the ANN models to map both classical (carboxylic oxygens) and nonclassical (halogen atom and aromatic ring π -electrons) H-bond acceptor sites

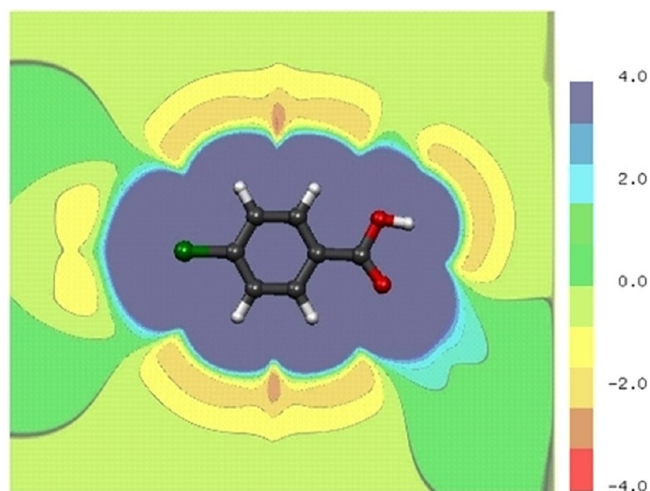


Figure 3. x,y -Plane through the hydrogen bond donor field (HDF) of *p*-chlorobenzoic acid in a 6 Å grid around atomic nuclei (values in kcal mol^{-1}).

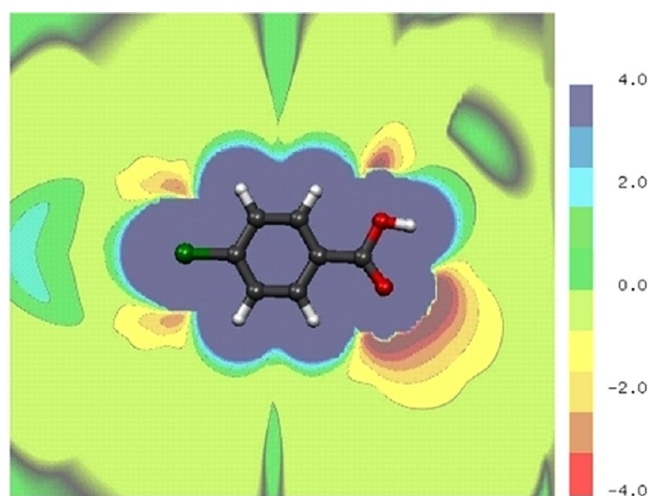


Figure 4. Contour map of the hydrogen bond acceptor field (HAF) of *p*-chlorobenzoic acid in the molecular plane and extending 6 Å outside the atomic positions (values in kcal mol^{-1}).

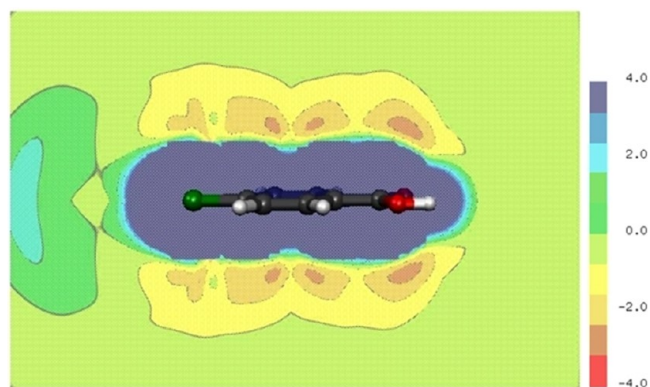


Figure 5. Contour map of the hydrogen bond acceptor field (HAF) of *p*-chlorobenzoic acid perpendicular to the molecular plane (values in kcal mol^{-1}).

(d). *Molecular Lipophilicity Potential (MLP)*. Hydrogen-bonding interactions are responsible for the ligand–target specificity. In contrast, hydrophobic interactions provide binding

strength.⁷ It has been shown that the single best structural parameter that correlates with binding affinity is the hydrophobic surface area that becomes buried on ligand binding.^{71,72} The MLP was used to describe this component of the binding interaction.

In classical additive models, the MLP defines the influence of all fragmental lipophilic contributions of a molecule on its environment, so the MLP value at a given point in the space around the molecule is the sum of the lipophilic intermolecular interactions between all the molecular fragments and the environment at this point.¹⁹ Therefore, to calculate the MLP, an incremental lipophilic contribution system (fragmental logP) and distance function are required. The MLP at point *r* around the molecule can be represented using eq 1

$$\text{MLP}(\mathbf{r}) = \sum_{i=1}^{N_{\text{frag}}} \mathcal{T}_i F(D_{ir}) \quad (1)$$

where N_{frag} is the total number of molecular fragments, \mathcal{T}_i the lipophilicity contribution (fragmental logP) of molecular fragment *i*, *F* the distance function, and D_{ir} the distance between fragment *i* and point *r*.

The MLP is therefore a function of logP, and it is not necessary to use a probe to calculate the MLP around the molecule as all the required information is implicit in logP.¹⁹ Several different methods for calculating the MLP in terms of molecular fragments and distance functions have been reported.^{19,73–76} Some use experimentally derived fragment contributions; others used parametrized ones. Hyperbolic^{73,75} and exponential^{19,74} distance functions have been proposed to represent the decay of the fragmental lipophilic contribution with distance from the molecule.

In previous work,⁷⁷ we described models that calculate the local hydrophobicity at the molecular surface. They assign a logP contribution to each surface patch. These models are based on local properties calculated at the standard isodensity surface using semiempirical MO theory and use descriptors obtained as the areas of the surface found in each bin in a predefined binning scheme. The integral over these surface points' logP contributions gives the overall logP of the molecule. In the current work, we used the best performing model (based on the AM1 Hamiltonian) to calculate the local lipophilicity and, unlike the previous published methods that used atomic fragment lipophilic increments to calculate MLP, we use the surface points' contribution, which should give a finer and more information-rich description of the MLP volume. To our knowledge, this is the first time that surface point lipophilicity has been used to calculate the MLP. We used Testa's distance function¹⁹ ($e^{-(R/2)}$) and have restricted the distance function by a cutoff of 4 Å to avoid the influence of too distant surface points

$$F(R) = e^{-(R/2)} \quad \text{for } R \leq 4 \text{ Å} \\ F(R) = 0 \quad \text{for } R > 4 \text{ Å} \quad (2)$$

We tested different distance functions and cutoffs and found these criteria to give the best correlation between $\sum \text{MLP}$ on the grid points and compound's experimental logP ($R^2 = 0.90$ and $\text{SEE} = 0.648$) using 1300 drug-like molecules (Supporting Information, 1). The MLP of grid points inside the van der Waals volume of the molecule was set to zero.

The MLP at point *r* around the molecule is calculated according to eq 3

$$\text{MLP}(\mathbf{r}) = \sum_{i=1}^{N_{\text{ti}}} P_i F(R_{ir}) \quad (3)$$

where N_{ti} is the total number of surface points, P_i the local lipophilicity (logP) of surface point *i*, and R_{ir} the distance between surface point *i* and point *r* around the molecule.

Figures 6 and 7 show the MLP of *p*-chlorobenzoic acid and illustrate its ability to distinguish positions around the molecule with positive (lipophilic) or negative (hydrophilic) MLP.

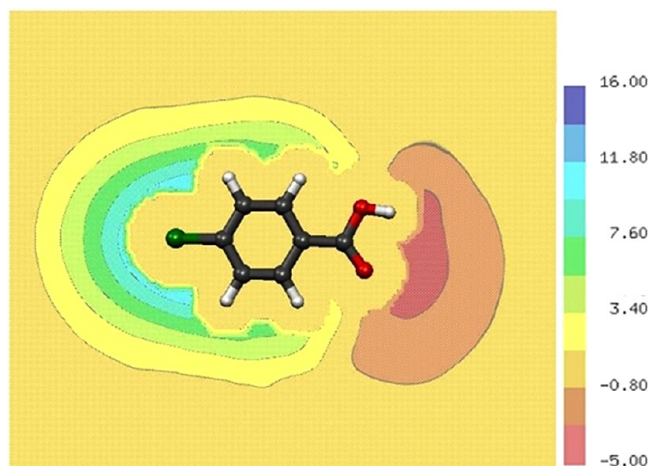


Figure 6. Contour map of the MLP of *p*-chlorobenzoic acid in the molecular plane and extending 6 Å beyond the atomic positions (kcal mol⁻¹ Å⁻²).

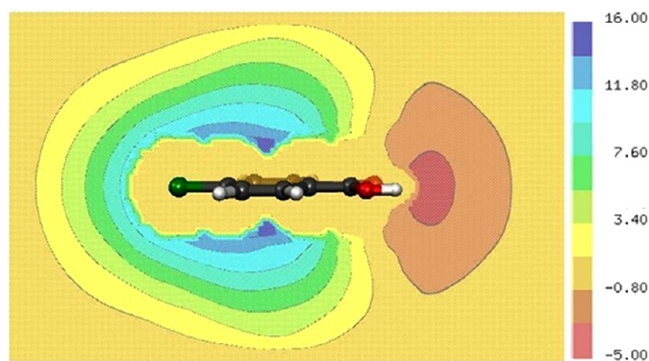


Figure 7. Contour map of the MLP of *p*-chlorobenzoic acid perpendicular to the molecular plane (kcal mol⁻¹ Å⁻²).

METHODS

Data Sets. 3D-QSAR methods generally require alignment of the molecules in the data sets. We therefore used data sets with reported alignments and 3D-QSAR performance, so that we can assess the performance of our approach in comparison to that of conventional 3D-QSAR techniques using the same alignments. Nine data sets were used; eight were originally compiled by Sutherland et al.⁷⁸ and the ninth by Matter et al.⁷⁹ These consist of the following. (1) A set of 114 angiotensin converting enzyme (ACE) inhibitors with pIC₅₀ values ranging from 2.1 to 9.9.⁸⁰ (2) A set of 111 acetylcholinesterase (AChE) inhibitors with pIC₅₀ values ranging from 4.3 to 9.5. (3) A set of 163 ligands for the benzodiazepine receptor (BZR) with pIC₅₀ values ranging from 5.5 to 8.9. (4) A set of 322 cyclooxygenase-2 (COX2) inhibitors with pIC₅₀ values that range from 4.0 to 9.0. (5) A set of 397

Table 1. Compound Distribution in the Sutherland et al. and Factor Xa Data Sets

	ACE	AchE	BZR	COX2	DHFR	GPB	THER	THR	fXa
training	76	74	98	188	237	44	51	59	80
test	38	37	49	94	124	22	25	29	27
inactives			16	40	36				

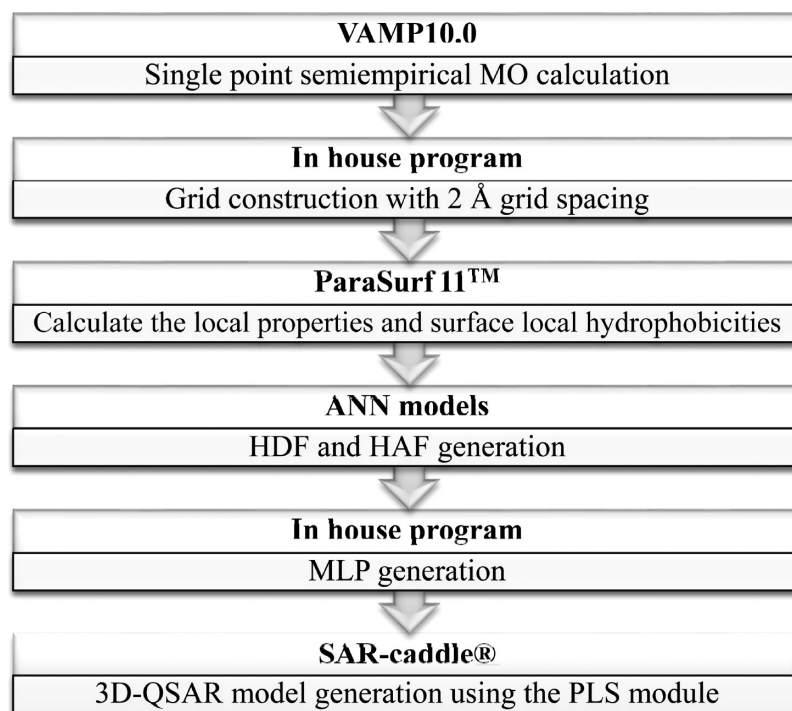


Figure 8. Workflow for 3D-QSAR model generation.

dihydrofolate reductase inhibitors (DHFR) with pIC_{50} values for rat liver enzyme ranging from 3.3 to 9.8. (6) A set of 66 inhibitors of glycogen phosphorylase b (GPB) with pK_i values ranging from 1.3 to 6.8.⁸¹ (7) A set of 76 thermolysin inhibitors (THER) with pK_i values ranging from 0.5 to 10.2.⁸¹ (8) A set of 88 thrombin inhibitors (THR) with pK_i values ranging from 4.4 to 8.5.⁸² (9) A set of 107 serine protease factor Xa (fXa) inhibitors with pK_i values ranging from 2.0 to 5.0.⁷⁹

The data sets were divided into training and test sets (and a set of inactive compounds in three data sets) in accordance with the original publications.^{78,79} Sutherland et al.⁷⁸ reported the performance of PLS models using CoMFA, CoMSIA basic (using steric and electrostatic fields), CoMSIA extra (CoMSIA models augmented by hydrogen bonding and/or hydrophobic fields), eigenvalue analysis (EVA),^{83–86} hologram QSAR (HQSAR),⁸⁷ traditional 2D-QSAR, and 2.5D-QSAR for the first eight data sets. For the BZR, COX2, and DHFR sets, they used several inactive compounds to assess if the QSAR models could identify them as low-activity compounds.⁷⁸ For the factor Xa (fXa) data set, a structure-based alignment for the ligands was employed by docking into the fXa crystal structure using the program QXP⁸⁸ based on a modified version of AMBER.⁸⁹ This was followed by optimization of the ligand geometries in the protein–ligand complex using the MMFF94s⁹⁰ force field prior to constructing CoMFA and CoMSIA models.⁷⁹ Table 1 shows the distribution of the compounds in each of the nine data sets.

Workflow for 3D-QSAR Model Generation Using QM-MIFs. The following workflow for 3D-QSAR model generation using QM-MIFs was used (Figure 8):

- Semiempirical MO calculation:** A single-point semiempirical MO calculation using the AM1 Hamiltonian was performed for each aligned molecule using VAMP10.0.⁹¹ (This step could be also performed using Mopac⁹² or EMPIRE⁹³). For this validation study, we did not perform semiempirical geometry optimization of the ligands to avoid changes in the reference alignments, and for each molecule we used the reported protonation state.^{78,79}
- Grid construction:** An in-house program was used to construct a 3D-grid around the aligned structures, which extends 4 Å in each direction beyond the atomic coordinates of all molecules and 2 Å grid spacing in accord with standard CoMFA procedures.⁷
- Calculation of the local properties and hydrophobicity of the surface points:** Using the VAMP10.0 output, ParaSurf 11⁹⁴ was used to calculate the electron density and the other local properties described above on the predefined grid points. ParaSurf also calculates the local hydrophobicity values for each molecule. (Local properties and their gradients at each grid point are required for calculating the HDF and HAF. These were calculated analytically using an in-house program that is now implemented in the latest version of ParaSurf).
- HDF and HAF generation:** An in-house program was used to generate the HDF and HAF for each molecule at each grid point using the corresponding ANN model⁵⁸ with the ParaSurf-calculated local properties and their gradients at this point.

- (e) **MLP generation:** Using the local hydrophobicity calculated by ParaSurf 11, an in-house program generates the MLP at each grid point according to eq 3.
- (f) **3D-QSAR model generation:** The PLS module in SAR-caddle⁹⁵ was used to generate the 3D-QSAR models based on the QM-MIFs (for details *vide infra*).

MIF Pretreatment and Model Generation. Pretreatment of the 3D-QSAR MIFs before model construction is a regular procedure to avoid singularities that prevent SAR trends from being identified or even compromise the formation of a predictive model completely.²⁴ In CoMFA, the pretreatment is performed such that the Lennard–Jones potential is truncated at a level of +30 kcal mol⁻¹, and the Coulomb potential is omitted accordingly.^{4,7} CoMSIA overcomes the singularities problem using Gaussian-type functions to generate smooth fields devoid of the very steep slope in close proximity to the atomic surface.^{5–7} Three of our MIFs (ρ , HDF, and HAF) exhibit this characteristic; grid points in close proximity to the atomic surface have very high field values. For the electron density, we used a cutoff of 10^{-5} e Å⁻³, as suggested by Güssregen et al.²⁴ Grid points with ρ values higher than this cutoff are set to 10^{-5} e Å⁻³. For HDF and HAF, different truncation levels were tested (0–20 kcal mol⁻¹), and no significant effect was found on the average performance of the nine data sets. Zero kcal mol⁻¹ was selected to be our default cutoff value because of the simplicity of the models obtained using this cutoff (fewer PLS components) and because it gave the best average performance in the test set prediction (lowest average standard error, for further details, see Supporting Information, 2). MIF values higher than the 0 kcal mol⁻¹ cutoff are set to the cutoff value.

For 3D-QSAR model generation, the individual QM-MIFs and their different combinations were tested to determine the combination that gives the best model for each data set. This also provides information about the MIFs important for ligand activity and binding to the biological target in each data set.

After pretreatment and prior to PLS analysis, the data is subjected to scaling, which assigns equal weight to all the MIFs and places them on a common basis for a meaningful statistical analysis. It improves the signal-to-noise ratio and also allows the relative importance of individual variables to be ranked.⁷ The scaling technique used here is similar to the CoMFA standard “block-scaling”,⁷ which scales the variables of each category (each field) to zero mean and unit standard deviation. The PLS module in SAR-caddle also performs data centering by subtracting the column means from all the column data. This does not change any coefficient values or comparative weights of the MIFs, but the number of significant components from PLS may be one less than from the data without centering, which improves the ease of interpretation and numerical stability.⁷

Statistical Analysis and Model Validation. Leave-one-out (LOO) cross-validation analyses,^{7,96–98} performed using the PLS module of SAR-caddle, were used to validate the model performance (internal validation). The maximum number of PLS components allowed was 12. The optimal number of PLS components was determined from the first minimum of the standard error obtained for the corresponding LOO PLS models (s_{LOO}). The best model among those of the individual QM-MIFs and their different combinations in each data set was selected as the one with the lowest LOO cross-validation standard error (s_{LOO}).

Furthermore, for the combinations of the number of PLS components and the blend of MIFs deemed most predictive

from LOO cross validation in each data set, the following were used: (a) 10-fold cross-validation (L10%O) was also carried out using the same combination to ensure the robustness and predictive ability of the model generated by this combination. (b) The final model was derived from the full training set and used to predict a test set (external validation), and the model performance was measured in terms of r^2_{test} and s_{test} . (c) Y-randomization (Y-scrambling) validation was carried out to ensure that a significant correlation indeed exists between the biological data and the combination of MIFs and that the model is not the result of a chance correlation. For this, 50 models were generated using the best combination after randomizing the biological activity vector between the compounds each time while keeping their original MIF set, and then the results of the original model were compared to the results of the Y-randomization models. (d) For the BZR, COX2, and DHFR sets, the set of inactive compounds was treated to assess the ability of the models to identify low-activity compounds, and the performance was measured by the percentage of compounds assigned as inactive. According to the original publication,⁷⁸ compounds in the inactive set were considered correctly classified by the models if the predicted activity was less than the average training set activity (pIC₅₀ values of 7.89, 6.98, and 6.23 for the BZR, COX2, and DHFR data sets, respectively). These criteria were considered appropriate by the authors of the original papers, but we have also added more stringent ones (the percentage of inactives found in the lowest 10 and 20 percentiles of compounds ordered according to their predicted activity).

The final PLS models obtained for the nine data sets were assessed by investigating their robustness and stability with respect to procedural variables such as grid resolution (grid spacing size) and grid orientation around the aligned molecules. The QM-MIF-based models CoMFA-like contour maps were analyzed to determine whether they can be used to identify the important molecular features required for binding. Finally, the QM-MIF-based models were also tested to determine if they could be used to identify trends in activity cliff compounds.⁹⁹

■ RESULTS AND DISCUSSION

Statistical Performance of QM-MIF-Based Models. In 3D-QSAR, the most useful measures of the model performance are the cross-validation and test set predictions as they measure the model's ability to predict the data and not just fit them.^{4,7,98} In this section, we focus on these criteria.

Sutherland et al. Data Sets. Table 2 shows the average performance of the different QSAR techniques. HDF and HAF were generated once using the H₂O-probe ANN models and once using the formamide-probe ANN models (see Supporting Information, 3, for detailed performance in each individual data set).

In the case of models generated using HDF and HAF from the H₂O-probe ANN models, the QM-MIF-based models show better average performance than the other QSAR techniques with q^2_{LOO} , $q^2_{\text{L10\%O}}$, and r^2_{test} of 0.59, 0.58, and 0.54, respectively, and s_{LOO} , $s_{\text{L10\%O}}$, and s_{test} of 0.80, 0.81, and 1.00, respectively, and even perform better than CoMSIA extra, which has the best average performance among the other QSAR techniques with q^2_{LOO} , $q^2_{\text{L10\%O}}$, and r^2_{test} of 0.58, 0.57, and 0.46, respectively, and s_{LOO} and s_{test} of 0.84 and 1.08, respectively. However, the QM-MIF models each use six components, compared with 4–5 for the classical models. For the models generated using HDF and HAF from the formamide-probe ANN models, the QM-based MIFs show slightly worse average performance than

Table 2. Average Performance of QM-MIF-Based (QMFA) Models on Eight Sutherland et al. Data Sets in Comparison to That of Conventional QSAR Approaches

	QMFA H ₂ O ^a	QMFA form ^b	CoMFA	CoMSIA basic ^c	CoMSIA extra ^d	EVA	HQSAR	2D	2.5D
NOC ^e	6	6	4	5	4	4	5	4	4
r^2_{train}	0.83	0.82	0.79	0.78	0.78	0.80	0.77	0.63	0.67
s_{train}	0.46	0.50	0.57	0.60	0.60	0.53	0.60	0.75	0.69
q^2_{LOO}	0.59	0.56	0.52	0.52	0.58	0.52	0.54	0.49	0.51
s_{LOO}	0.80	0.84							
$q^2_{\text{L10\%O}}$	0.58	0.55	0.52	0.49	0.57	0.50	0.52	0.48	0.49
$s_{\text{L10\%O}}$	0.81	0.86	0.88	0.90	0.84	0.89	0.87	0.90	0.88
r^2_{test}	0.54	0.50	0.43	0.37	0.46	0.31	0.33	0.20	0.25
s_{test}	1.00	1.06	1.10	1.17	1.08	1.22	1.18	1.31	1.28
%inact. ^f	81.7	79.7	75.3	72.7	76.7	69.7	73.3	73.7	79.7
%inact. ^g 10%	6	20	39						
%inact. ^g 20%	31	35	58						
Ran r^2_{aver} ^h	0.35	0.38							
Ran r^2_{max} ⁱ	0.63	0.65							
Ran q^2_{LOOaver} ^j	0.05	0.05							
Ran q^2_{LOOmax} ^k	0.21	0.22							

^aHDF and HAF were generated using H₂O-probe ANN models. ^bHDF and HAF were generated using formamide-probe ANN models. ^cUsing steric and electrostatic fields only. ^dIncluding hydrogen bonding and/or hydrophobic fields as well. ^eAverage number of PLS model components. ^fAverage % of correct prediction for the three data sets of inactive compounds for BZR, COX2, and DHFR using the criteria employed in the original publications. ^gAverage % of correct prediction for the three data sets of inactive compounds for BZR, COX2, and DHFR assigning the weakest 10 or 20 percentiles as inactive. ^hAverage r^2 of the 50 Y-randomization models. ⁱMaximum r^2 in the 50 Y-randomization models. ^jAverage q^2_{LOO} of the 50 Y-randomization models. ^kMaximum q^2_{LOO} in the 50 Y-randomization models.

for the H₂O-probe-based models with q^2_{LOO} , $q^2_{\text{L10\%O}}$, and r^2_{test} of 0.56, 0.55, and 0.50, respectively, and s_{LOO} , $s_{\text{L10\%O}}$, and s_{test} of 0.84, 0.86, and 1.06, respectively. However, these values are still better than the other QSAR techniques and comparable to CoMSIA extra. Thus, independently of the absolute performance of 3D-QSAR methods for the data sets considered using the QM-MIFs leads to an improvement in the average r^2_{train} and r^2_{test} values. Note that these improvements are statistically significant as the direct comparison is between CoMFA with QM-MIFs and classical CoMFA (rather than CoMSIA). It is likely that using the QM-MIFs in a CoMSIA-like approach would give better results, although we have not tested this possibility.

In both cases, using the more rigorous 10-fold cross-validation instead of the LOO cross-validation does not change the overall results (q^2_{LOO} vs $q^2_{\text{L10\%O}}$ = 0.59 vs 0.58 and s_{LOO} vs $s_{\text{L10\%O}}$ = 0.80 vs 0.81) in the H₂O-based models and (q^2_{LOO} vs $q^2_{\text{L10\%O}}$ = 0.56 vs 0.55 and s_{LOO} vs $s_{\text{L10\%O}}$ = 0.84 vs 0.86) in the formamide-based models, indicating the robustness and stability of the resulting PLS models.

Table 2 also shows that H₂O-based models surpass all others in predicting the inactive compounds in the BZR, COX2, and DHFR data sets, while the formamide-based models predicted them better than the other QSAR techniques except 2.5D, which has the same average prediction percentage.

Y-scrambling validation showed that the model selected for each data set represents a significant correlation between the biological activity and the QM-MIFs used and is not a statistical chance correlation. This is clearly demonstrated by the significant difference between the original model q^2_{LOO} and the 50 Y-randomization models average and maximum q^2_{LOO} in each data set (Supporting Information, 3, Table 3), and so we are confident that the QM-MIF-based models obtained can be used reliably for SAR trend extraction.

We will focus our detailed comparison on the results of the 3D-QSAR approaches that are analogous to ours (CoMFA, CoMSIA basic, and CoMSIA extra) and use the results from the

Table 3. Performance of QM-MIF Models on Factor Xa Inhibitors Data Set in Comparison to That Reported for CoMFA and CoMSIA

	QMFA H ₂ O ^a	QMFA form ^b	CoMFA	CoMSIA
NOC ^c	4	4	6	5
MIFs ^d	HDF, HAF, MLP	HDF, HAF, MLP		
r^2_{train}	0.91	0.91	0.95	0.90
s_{train}	0.28	0.26		
q^2_{LOO}	0.68	0.71	0.74	0.61
s_{LOO}	0.51	0.49	0.51	0.59
$q^2_{\text{L10\%O}}$	0.68	0.73		
$s_{\text{L10\%O}}$	0.51	0.47		
r^2_{test}	0.75	0.75	0.73	0.78
s_{test}	0.41	0.41		
Ran r^2_{aver} ^e	0.54	0.49		
Ran r^2_{max} ^f	0.76	0.73		
Ran q^2_{LOOaver} ^g	0.07	0.06		
Ran q^2_{LOOmax} ^h	0.29	0.29		

^aHDF and HAF were generated using H₂O-probe ANN models. ^bHDF and HAF were generated using formamide-probe ANN models. ^cNumber of PLS components used in the model. ^dMIF combination that gave the best model. ^eAverage r^2 of the 50 Y-randomization models. ^fMaximum r^2 in the 50 Y-randomization models. ^gAverage q^2_{LOO} of the 50 Y-randomization models. ^hMaximum q^2_{LOO} in the 50 Y-randomization models.

models used HAF and HDF generated employing the H₂O-probe ANN models.

Figures 9 and 10 compare the q^2_{LOO} and r^2_{test} for the QM-MIF-based (QMFA) models with those of the other 3D-QSAR approaches for the Sutherland et al. data sets.⁷⁸ The QM-MIFs perform better than CoMSIA basic for all the data sets in both the internal and external validations; however, the superiority is more pronounced in the external validation.

In comparison to CoMFA, the QM-MIFs perform better in the LOO cross validation in seven data sets and slightly worse for

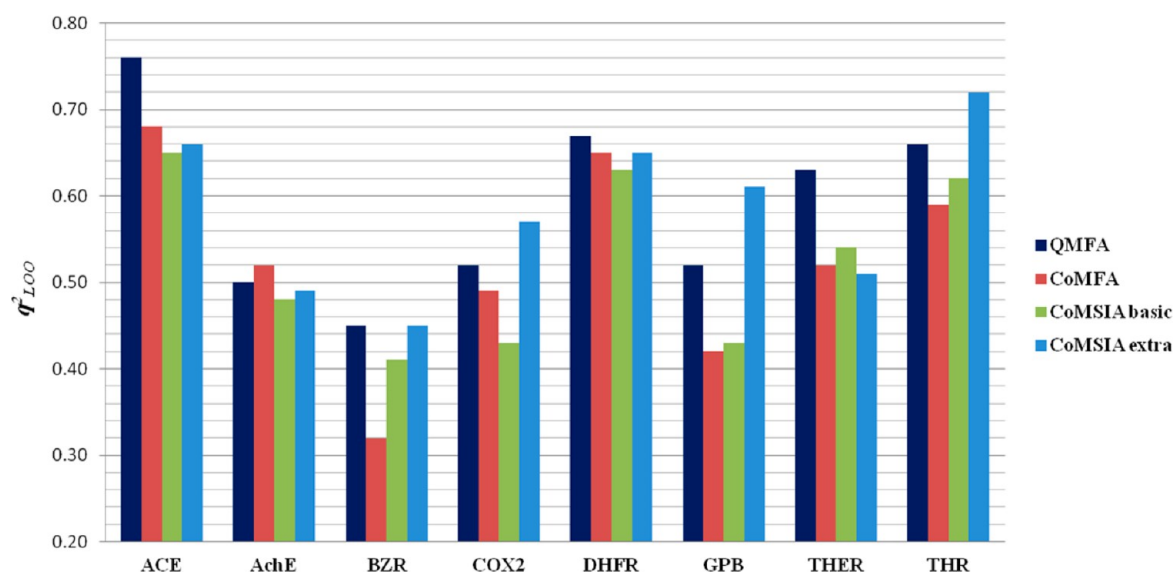


Figure 9. q^2_{LOO} for the different data sets for 3D-QSAR approaches.

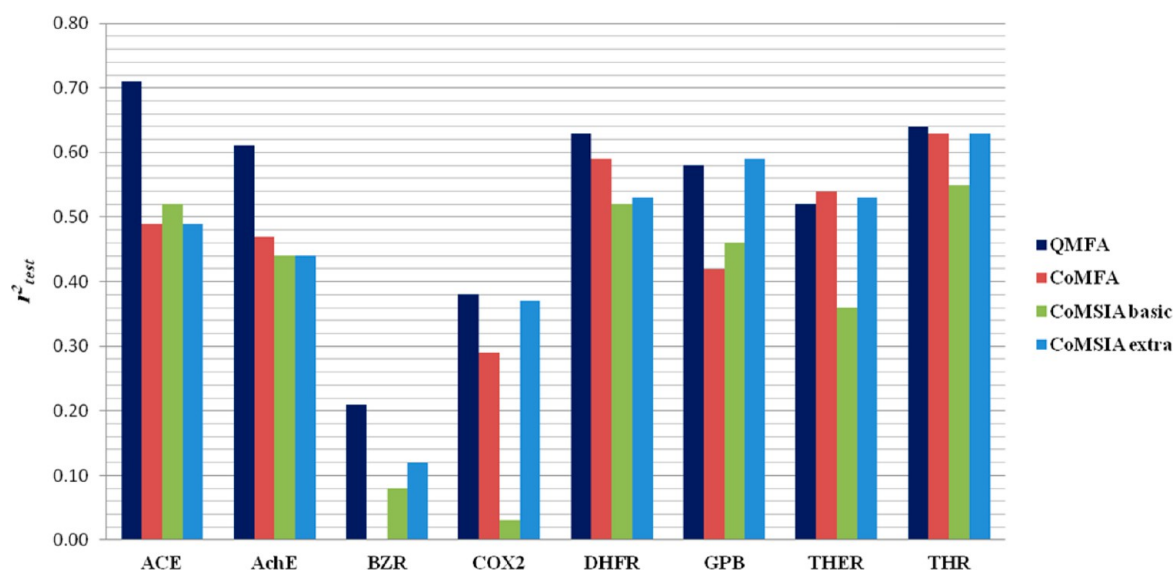


Figure 10. r^2_{test} for the different data sets for 3D-QSAR approaches.

AchE. However, the test-set prediction for this data set is significantly better than that given by all other methods.

In comparison to CoMSIA extra, QM-MIFs perform better in the internal validation for four data sets and equally well for BZR, while for COX2, GPB, and THR they are slightly worse. However, Figure 10 shows that the test-set predictions of the QM-MIF models again show significantly better performance for four data sets, while for COX2, GPB, THER, and THR, they perform approximately as well as CoMSIA extra.

These results suggest that the information contained in the QM-MIFs is more complete, more accurate, or better resolved than the traditional CoMFA fields. The improvement found is approximately that expected; using the QM-MIFs improves the performance of a CoMFA-like technique to that of conventional CoMSIA extra or better.

These results suggest that the QM-MIF models perform better than, or as well as, the conventional approaches. It is particularly encouraging that the relative performance of the QM-MIF

models improves for the test sets, which suggests that the models are robust.

Factor Xa Inhibitor Data Set. Model generation was carried out using HDF and HAF generated once using H₂O-probe ANN models and once using formamide-probe ones. Table 3 shows the performance of the best model in each case in comparison to that reported⁷⁹ for CoMFA and CoMSIA. Both models are characterized by four PLS components, which is less than reported for CoMFA and CoMSIA (6 and 5 components, respectively), indicating that the equations obtained are simpler and less liable to potential overfitting. Nevertheless, r^2_{train} for the QMFA models is comparable to those of CoMFA and CoMSIA, indicating that the individual QM-MIF based components contain more information. The best models generated are based on HDF, HAF, and MLP MIFs (Table 3) indicating the importance of such fields, which agrees well with the published data⁷⁹ for the best CoMSIA model obtained, in which the contribution of the electrostatic field was 48% and that of the

hydrophobic field 36% while the steric field had a minor contribution of 16%.

In terms of q^2_{LOO} and s_{LOO} , the formamide-probe based H-bond MIFs yield marginally better models than the H₂O-probe based ones (q^2_{LOO} of 0.71 vs 0.68 and s_{LOO} 0.49 vs 0.51, respectively), but both perform better than the CoMSIA model (q^2_{LOO} = 0.61 and s_{LOO} = 0.59). Despite having a slightly lower q^2_{LOO} than that of CoMFA (0.74), their s_{LOO} is similar to that of CoMFA (0.51 for CoMFA), suggesting that the models have similar predictive ability. The performance of both QM-MIF based models on the test set is the same (r^2_{test} = 0.75 and s_{test} = 0.41) and comparable to that of CoMFA and CoMSIA (r^2_{test} = 0.73 and 0.78, respectively), indicating that all the models have similar predictive ability. Figure 11 shows the experimental vs the predicted

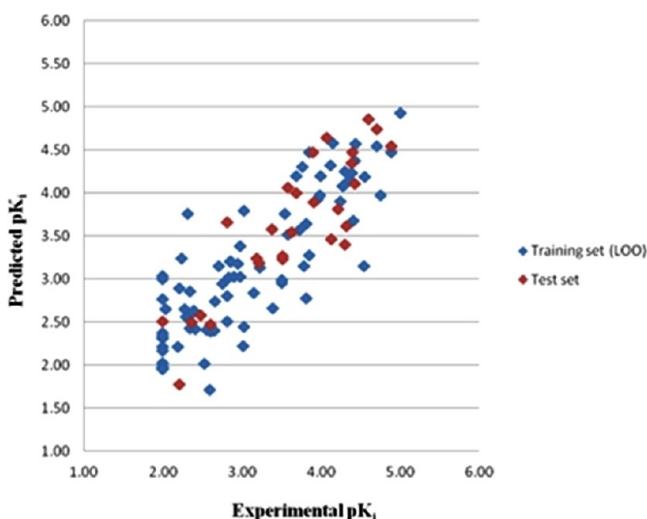


Figure 11. Experimental vs predicted pK_i for the training set in the LOO cross-validation and for the test set using the model generated using HDF and HAF from the formamide-probe ANN models.

pK_i plot for the training set in the LOO cross-validation and for the test set using the model generated using HDF and HAF with the formamide-probe ANN models (see Supporting Information, 4, Figure 4 for the H₂O-probe based models)

Further validation of the models generated using the more rigorous 10-fold cross-validation showed no significant effect on the performance (Table 3), indicating the robustness and stability of the models. The Y-randomization test also showed that the models obtained are unlikely to result from chance correlation, as indicated by the significant difference between the true models' performance and the average and maximum q^2_{LOO} of the 50 Y-randomization models (Table 3). It also shows that the true value for the models obtained are separated from the "background" scrambled reference distribution (see Supporting Information, 4, Figure 5 for the formamide-probe based models and Figure 6 for the H₂O-probe based models).

Robustness and Stability with Respect To Model Building Variables. 3D-QSAR models may vary strongly with small changes in the calculation protocol. We therefore tested the effect of two variables, the grid resolution (grid spacing size) and grid orientation around the aligned structures, which can sometimes influence the results of conventional 3D-QSAR. For example, varying the grid orientation in conventional CoMFA may change q^2 by 0.5 units.^{100,101}

Effect of Grid Resolution (Grid Spacing Size). To investigate the effect of the grid spacing, models were generated

using the HDF and HAF combination generated using the H₂O-probe ANN models (Supporting Information, 3, and Table 3) with systematic variation of the grid resolution from 1.0 to 5.0 Å in 0.5 Å increments. The average performance of the QM-MIF based models for the different data sets in terms of q^2_{LOO} and r^2_{test} decreases very slowly and smoothly with increasing grid size. The opposite slight change is found for s_{LOO} and s_{test} (Figures 12 and 13).

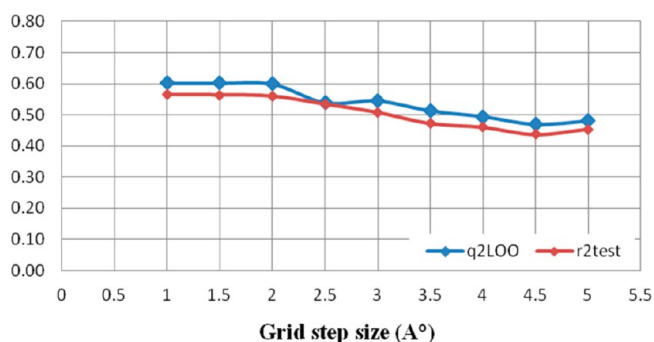


Figure 12. Effect of the change in grid spacing size on the average q^2_{LOO} and r^2_{test} .

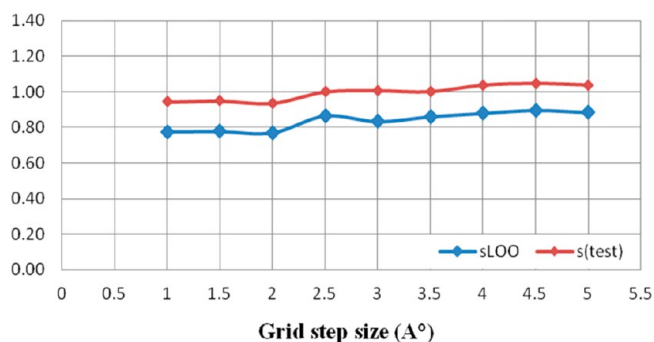


Figure 13. Effect of the change in grid spacing size on the average s_{LOO} and s_{test} .

These results indicate that the models are robust and stable and that 2 Å is the optimum grid spacing size in term of performance and computational demand. Some data sets showed more sensitivity than others to changes in grid spacing size. GPB and THER were the most sensitive (q^2_{LOO} SD = 0.12 and 0.13, respectively) (Supporting Information, 5).

Effect of Change in Grid Orientation around Aligned Molecules. The overall orientation of the superimposed molecules without affecting individual alignments in each data set was varied as follows. Starting from the original orientation,^{78,79} using an in-house program, the whole alignment was rotated by 15° at a time around the y axis up to 180°, and a new grid was constructed that extends 4 Å in each direction beyond all molecules with 2 Å spacing. For the new orientations, models were generated using the same MIF combinations as for the test of grid spacing. Figures 14 and 15 show the stability and robustness of the QM-MIF based models to changes in grid orientation. This is indicated by the unaffected average performance of the models in the different orientations (q^2_{LOO} max = 0.61, q^2_{LOO} min = 0.54, standard deviation = 0.02, s_{LOO} min = 0.77, s_{LOO} max = 0.84, and standard deviation = 0.03).

GPB and THER were again found to be the most sensitive (q^2_{LOO} SD = 0.10 and 0.11, respectively) (Supporting Information, 6), indicating that these two data sets are very sensitive to changes

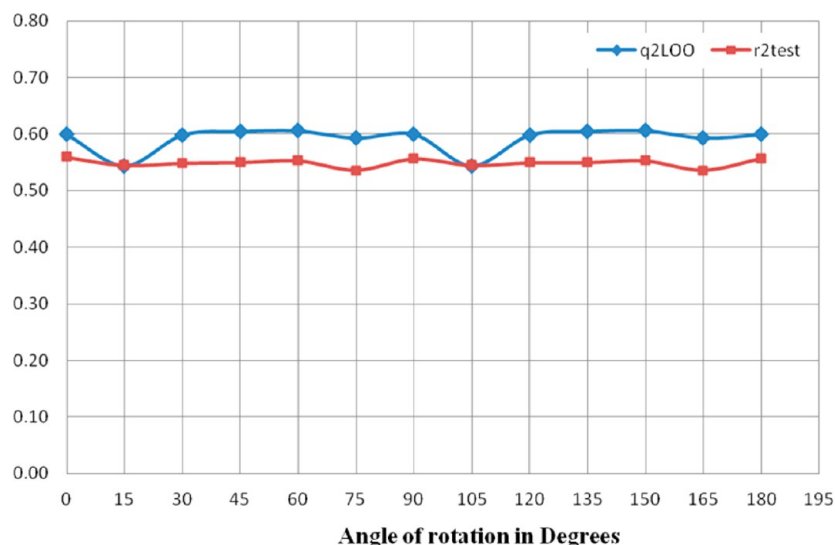


Figure 14. Effect of the change in grid orientation on the average q^2_{LOO} and r^2_{test} .

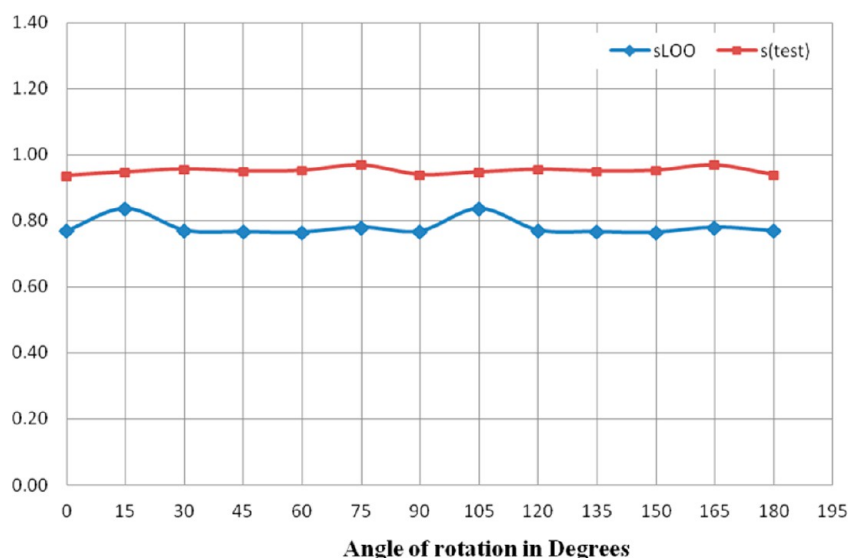


Figure 15. Effect of the change in grid orientation on the average s_{LOO} and s_{test} .

in the protocol. This should be considered when using these two data sets in future 3D-QSAR validation exercises.

Interpretability of QM-MIF Contour Maps. One important goal of 3D-QSAR is to identify relevant chemical features linked to the biological activity. This led us to investigate the chemical interpretation of the QM-MIF contour maps from the corresponding QSAR models. Therefore, contour maps for the factor Xa 3D-QSAR model based on HDF and HAF generated using H₂O-probe ANN models were constructed using 2 Å grid spacing. Those were inspected and interpreted and compared to the known information from the corresponding X-ray crystal structure (PDB 2BMG, resolution 2.7 Å) in complex with compound **50** ($K_i = 18$ nM) from this data set (Figure 16) (numbering according to the original publication⁷⁹).

The factor Xa protein binding site is subdivided into three regions,⁷⁹ as shown in Figure 16.

Subsite S1. The inhibitor dichlorophenyl moiety is located in this S1 subsite, where the *para*-chlorine atom is involved in a halogen- π interaction with the center of the aromatic ring of

Tyr228 at the rear wall of S1.¹⁰² This interaction is additionally stabilized, as the chlorine atom displaces one structurally conserved water molecule, which is usually found in fXa X-ray structures of ligands with a benzamidine moiety in S1.¹⁰³ This position of the water molecules agrees to the single very high excess chemical potential hydration site that solvates Tyr228 in the S1 pocket. Several studies have shown that displacing the water molecule from this position by a ligand halogen atom is very favorable for binding affinity; the energetic consequences of water displacement were studied by Abel et al.¹⁰³ The *ortho*-chlorine atom, on the other hand, is solvent-exposed and interacts with the O γ atom of the inward-directed Ser195 side chain.

Central Region and Ester-Binding Pocket, EBP. The 3-oxybenzamide aromatic ring is located in this central position with its nitrogen atom H-bonded to the carbonyl oxygen of Gly216, and the 4-methoxy moiety is located in the EBP on top of the Cys191–Cys220 disulfide bridge and surrounded by the Arg143, Glu147, and Gln192 side chains adjacent to S1.

Subsite S4. In this subsite, the pyridyl moiety is situated between the aromatic side-chains of Tyr99 and Phe174

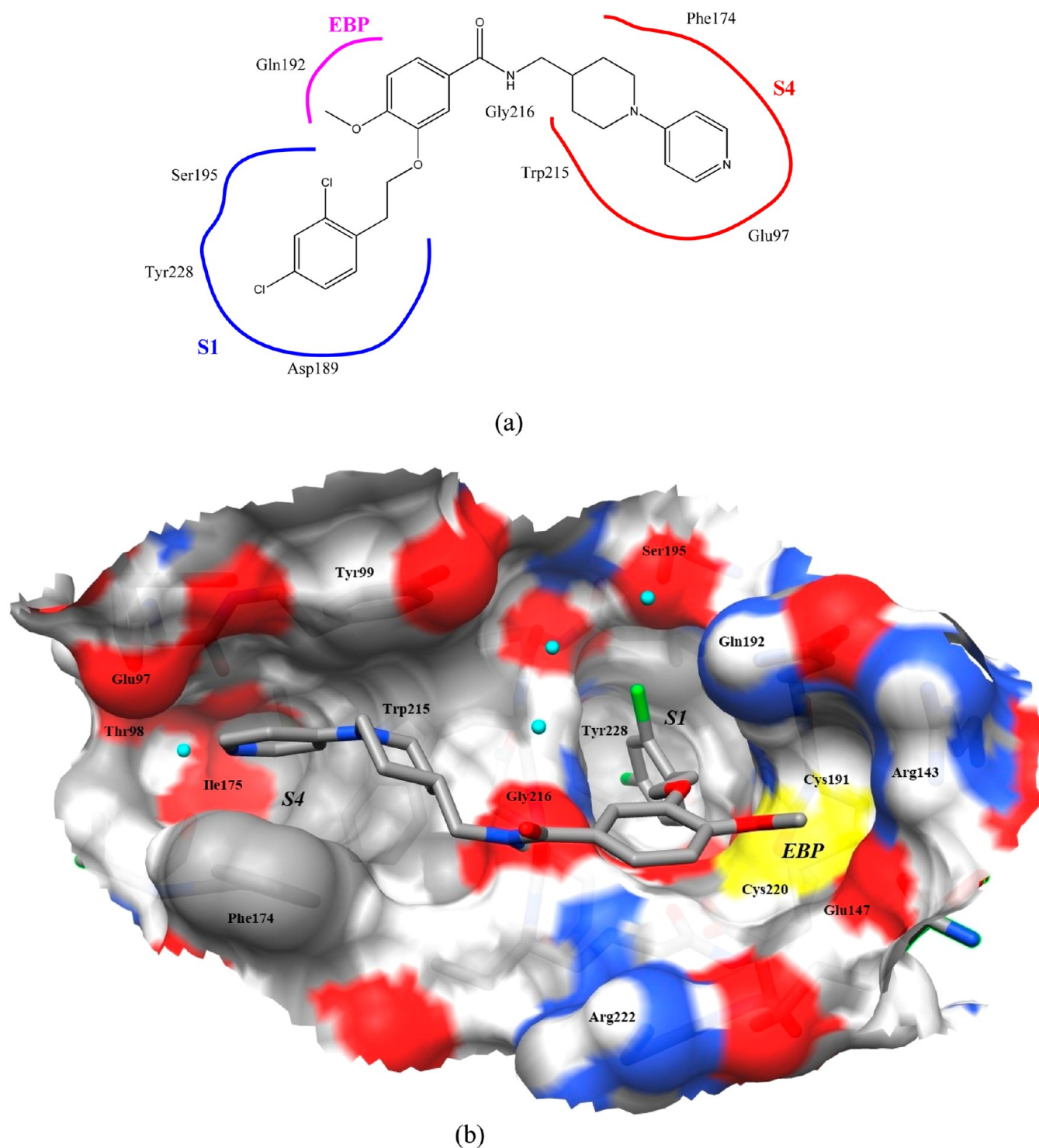


Figure 16. Binding mode of compound 50 in the binding site of human factor Xa: (a) in 2D representation (adapted from ref 78) and (b) in 3D representation. The binding site is shown as the solvent-excluded surface color-coded by element-type (C, gray; H, white; O, red; N, blue; and S, yellow). Structurally conserved water is displayed in cyan. Nonpolar hydrogen atoms are omitted for clarity.

with its nitrogen involved in an H-bond network via a structurally conserved water molecule in S4 with the Thr98 carbonyl oxygen and hydroxyl group and the Ile175 carbonyl oxygen.

One structurally conserved water atom is present in the PDB structure 2BMG near Gly216-N but at a longer distance than that expected for hydrogen-bonds. The 3.94 Å distance from Gly216-N to the water is too long for a close contact H-bond in this structure,

while other fXa X-ray structures from the same series reveal similar water molecules in this region as close as 3.26 Å to Gly216-N, thus possibly within hydrogen-bonding distance. This particular water molecule in the PDB 2BMG is part of a network with two other water molecules contacting the side chain of Ser195.

As shown in Table 3, the best 3D-QSAR model for fXa inhibitors involved HDF, HAF, and MLP MIFs, which is

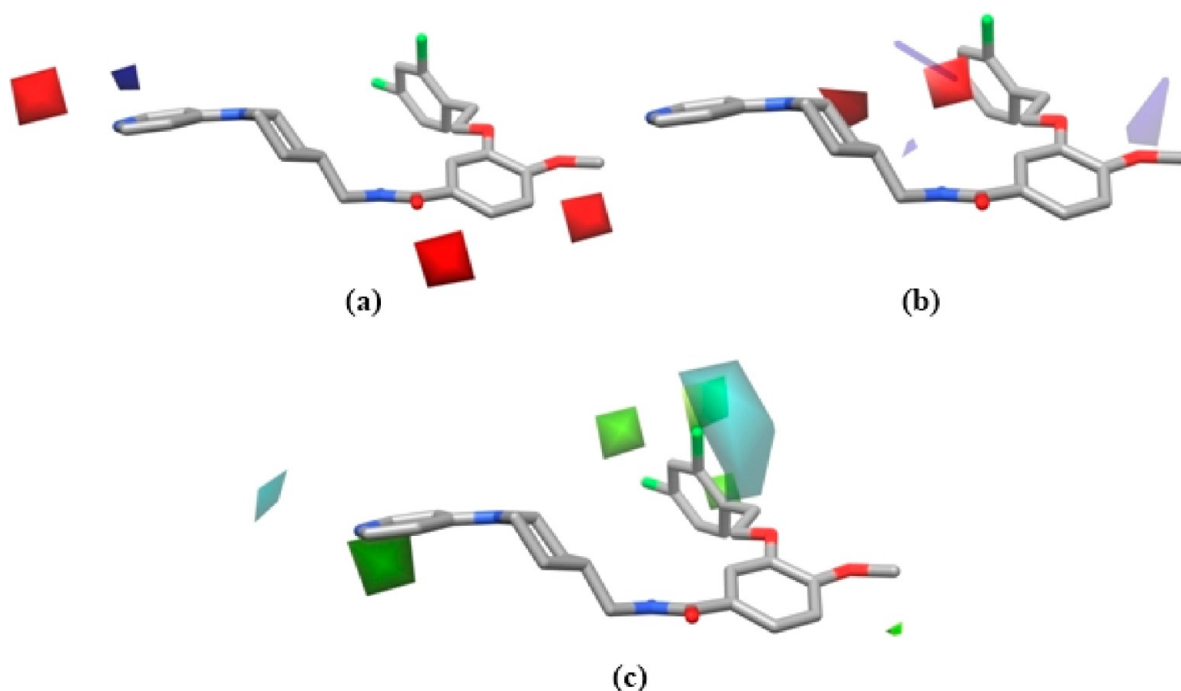


Figure 17. Contour maps with compound 50 ($K_i = 18$ nM).⁷⁹ Nonpolar hydrogen atoms are omitted for clarity. (a) The coeff^*std contour map for the HAF. Red contours (<-0.034) refer to regions where a hydrogen-bond acceptor is favorable for affinity, while blue contours ($>+0.025$) indicate those where a hydrogen-bond acceptor is disfavored. (b) The coeff^*std contour map for the HDF. Red contours (<-0.023) refer to regions where a hydrogen bond donor is favorable for affinity, and blue ($>+0.023$) indicates those where a hydrogen bond donor is disfavored. (c) The coeff^*std contour map for MLP. Green contours ($>+0.0159$) refer to regions where hydrophobic substituents are favorable for affinity, and cyan (<-0.018) indicates those where they are not favorable.

consistent with the criteria required for the binding mode, as indicated above.

Figure 17 shows contour maps for each contributing field mapped onto the experimental binding pose of compound 50. The coeff^*std contour maps were derived from the PLS coefficients at each grid point. As for CoMFA MIFs, the interactions of the ligand in the case of our QM-MIFs are found at positions of potential partners in the biological target, i.e., they project the favorable interactions toward the protein binding site.

Figure 17a shows the coeff^*std contour map for the HAF. A red contour region in front of the pyridyl-nitrogen indicates its favorable involvement as H-bond acceptor in a H-bond interaction, as revealed by the X-ray structure of the fXa /50 complex by contacting a structurally conserved water molecule at the edge of the S4 subsite. A red contour below and in front of the carbonyl oxygen atom of the benzamide indicates a favorable location of an H-bond acceptor in this area. Despite the absence of direct interaction with any part of the fXa binding site in this position, the conclusion drawn in the interpretation of this SAR model contour map is the favorable position and orientation of the entire *trans*-amide group with the NH involved as donor in a favorable H-bond to Gly216-C=O (see below) and the *trans*-carbonyl pointing toward the bulk solvent. An area of favorable interaction below and in front of the oxygen of the 4-methoxy group indicates a favorable interaction between this oxygen as a negatively charged group with the EBP, which is consistent with observations from CoMFA and CoMSIA electrostatic fields that an increase in negative charge is preferable at position 4 of the benzamide scaffold. This agrees with the observation that halogen substituents in this area are favorable for binding affinity. A blue contour in front of the inward *ortho*-hydrogen of the pyridyl ring indicates that the presence of an H-bond acceptor in this position

is disfavored due to the presence of the Ile175-C=O, Thr98-C=O, and OH oxygen atoms surrounding this region.

Figure 17b shows the coeff^*std contour map for the HDF. The red contour in front of the benzamide amino-group indicates its involvement as H-bond donor in an interaction with Gly216-C=O as H-bond acceptor in the fXa binding site. Another red contour is found close to the piperidyl nitrogen atom, directly at the optimal position for a favorable interaction to the Trp215 indole π system. A blue contour above in the front of the 4-methoxy oxygen indicates the disfavored presence of H-bond donor in this position because of the presence of hydrogen atoms of Gln192-NH₂ at this position.

Figure 17c shows the coeff^*std contour map for MLP. Green contours around the dichlorophenyl moiety and its *p*-chlorine atom indicate their involvement in a hydrophobic interaction responsible for increased affinity, in agreement with the X-ray crystal structure, which suggests that the dichlorophenyl moiety replaces the structurally conserved water in this hydrophobic S1 site leading to increased affinity,^{103,104} and that the *p*-chlorine atom is involved in a favorable Cl... π hydrophobic interaction with the orthogonal aromatic ring of Tyr228. On the other hand, the solvent-exposed *ortho*-chlorine atom is surrounded by a cyan contour, which indicates that hydrophilic substituents at this position might be favorable. This could be attributed partially to interactions pointing toward the hydroxyl group from the active triad residue Ser195-OH. Despite being open to the bulk solvent, the small green contour around the 4-methoxy CH₃ moiety suggests its possible favorable interactions with the lipophilic parts of the side chains of Glu143 and Arg222. A green contour below the pyridyl ring represents the favorable π -stacking interaction³² with the aromatic residues of Phe174 and Trp215 lining the S4 pocket. A cyan contour directly in

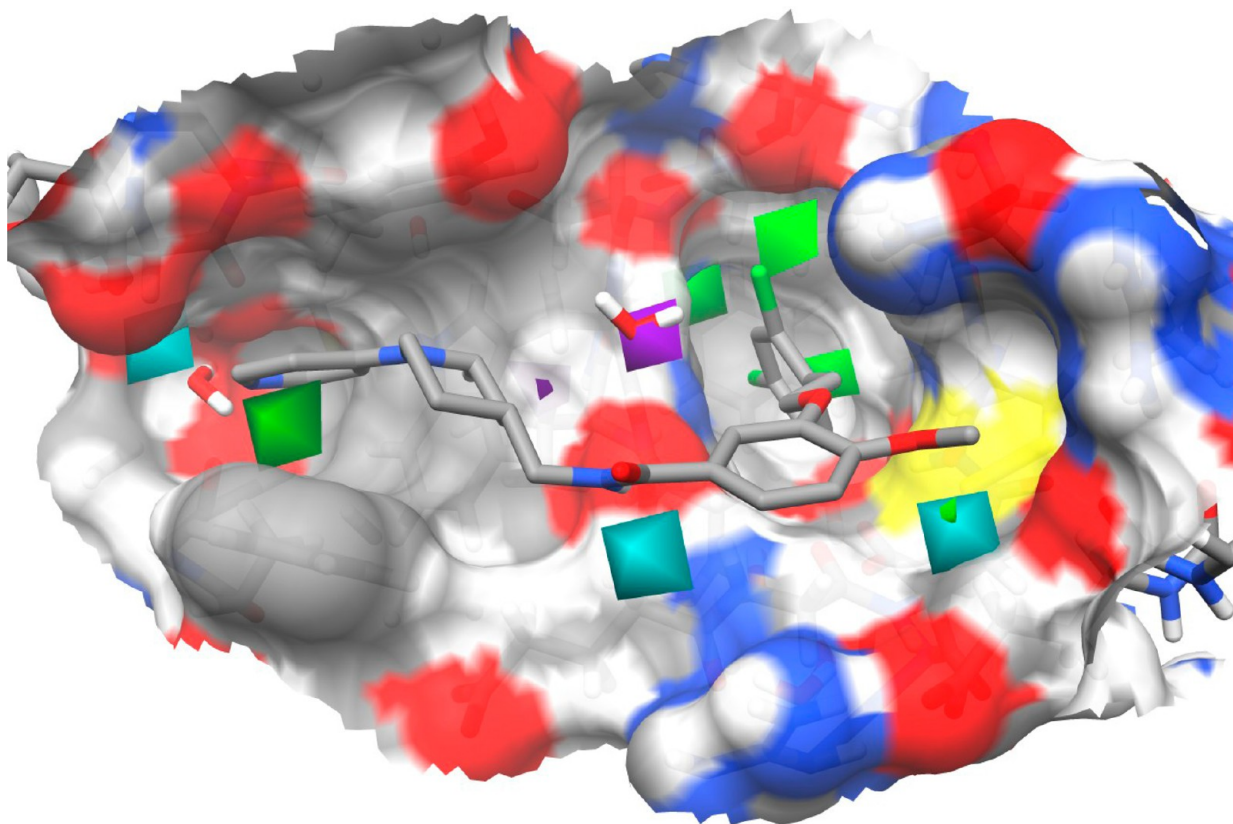


Figure 18. Contour maps with compound 50 ($K_i = 18 \text{ nM}$)⁷⁹ within the factor Xa binding site solvent-excluded surface to show its agreement to characteristics of the serine protease binding site. Nonpolar hydrogen atoms are omitted for clarity. Cyan contours refer to coeff*std contour map for the HAF (<-0.034) where hydrogen bond donors in the binding site are expected. Purple contours refer to coeff*std contour map for the HDF (<-0.023) where hydrogen bond acceptors in the binding site are expected. Green contours refer to coeff*std contour map for the MLP ($>+0.0159$) where hydrophobic substituents in binding site are expected.

Table 4. Percentage of Activity Cliff Pairs Whose Trend Was Correctly Predicted in Each Data Set

	ACE	AchE	BZR	COX2	DHFR	GPB	THER	THR	fXa
% of pairs that contain test-set compounds	60	0	50	10	10	30	40	60	100
% correct trend predictions	70	80	50	100	80	70	80	90	100
% correct separation by <1 log unit	50	50	40	70	70	30	60	20	30
% correct separation 1–2 log units	20	30	10	30	10	40	20	20	50
% correct separation >2 log units								50	20

front of the pyridyl nitrogen indicates its involvement in a hydrophilic interaction in this position, in agreement with the previous finding from the HAF contour map and the experimental binding mode.

Figure 18 shows the contour maps of the favorable interactions around compound 50 placed within the factor Xa binding site. One magenta-colored contour region indicating favorable interactions from HDF is found to be located at the position of this structural water molecule in the center of Figure 18, thus indicating favorable contributions from a ligand H-donor functionality, which could possibly contact this conserved water molecule. From both energy minimization and a comparative analysis of X-ray structures in this series, it can be concluded that the plane and position of the amide bond linking the central phenyl ring to the piperidyl moiety is flexible and can move more toward this water molecule, thereby avoiding a close contact to the receptor Gly219–NH. However, this slight shift also affects the hydrogen bond to Gly216–C=O. In summary the ideal geometrical arrangement and orientation of

this ligand amide plane is indicated by the magenta color for the ligand NH and the cyan contour for the carbonyl oxygen. All in all, Figure 18 shows the agreement between the QM-MIF based contour maps and the X-ray structure binding mode characteristics, demonstrating the ability of the QM-MIF based contour maps to predict the key binding requirements in the ligands and highlight the corresponding binding characteristics in the target protein.

Validation of Ability of QM-MIF-Based Models To Differentiate between Activity Cliff Compounds. Activity cliff compounds are pairs of compounds in the QSAR data sets have similar chemical structures but differ significantly in their biological activity.⁹⁹ Although they sometimes reveal crucial features required for activity, inadequate QSAR models predict those compounds as statistical outliers.¹⁰⁵ QSAR models capable of differentiating between these activity cliff compounds are important as they can capture the structural features required for the biological activity in difficult cases. In general, “activity

cliffs" are simply an indication that the descriptors used in a model are inadequate because they result in discontinuities in the SAR.

To validate the ability of our models to differentiate between those compounds, for each data set the most significant 10 activity cliff pairs were determined based on the structure–activity landscape index (SALI)⁹⁹ value (see Supporting Information, 7, for detailed description of the procedures used to determine the activity cliff pairs). The predicted biological activity for these compounds in LOO cross-validation (if they were used in the training set) or in the test set (if in the test set) was used to calculate the percent of the pairs whose trend was predicted correctly. This parameter was used to validate the models efficiency as shown in Table 4.

Table 4 shows that the models can predict the biological activity trend of the different activity cliff pairs well in all the data sets except BZR. As expected, the BZR model cannot differentiate between the activity cliff pairs because of its poor statistical performance for the entire data set, as shown in Figures 9 and 10 and the Supporting Information, 3.

CONCLUSIONS

Being quantum mechanics based, the QM-MIFs are less arbitrary and more general than the currently available force field-based ones and can, for instance, describe intermolecular interactions that cannot be described by atom-centered charge models. Despite their QM origin, they can be calculated rapidly using semiempirical MO theory and are thus suitable for high-throughput applications. The QM-MIFs showed an overall statistically better performance than conventional QSAR approaches for the data sets investigated. In fact, they perform significantly better than the other approaches for most of the data sets used (ACE, AchE, BZR, DHFR, and THER). This superiority is more pronounced for test-set prediction (external validation), which is the most important criterion for judging the quality of the QSAR model and indicates the extrapolative predictivity of the models generated. The different validation approaches used, LOO, 10-fold cross-validation, and external validation showed the robustness and stability of the models obtained, and the Y-randomization test showed that the models obtained are due to significant correlation between the QM-MIFs and biological activity rather than statistical chance. There is no clear indication that a particular combination of fields performs consistently better than the others. We conclude that the selection of an optimal MIF combination depends on the data set investigated and the forces involved in the binding to the biological target. The QM-MIF-based models are stable to changes in the computational protocol such as the grid spacing size and orientation around the aligned molecules. The QM-MIF-based contour maps can be interpreted easily and are consistent with the binding requirements extracted from the experimental binding mode in the X-ray structure. These characteristics together indicate significant advantages of QM-MIFs compared to their classical counterparts. Finally, the QM-MIFs are able to distinguish between "activity cliff" pairs well, revealing the origin of "activity cliffs" as a simple descriptor deficiency.

ASSOCIATED CONTENT

Supporting Information

(1) Correlation between \sum MLP of all grid points and compounds' experimental logP. (2) Effect of the HDF and HAF truncation level on the data sets performance. (3) Performance of the QM-MIFs (QMFA) models on the eight Sutherland et al. data

sets. (4) Performance of the QM-MIFs-based model of factor Xa inhibitor data set. (5) Effect of the change in grid spacing size on the QM-MIFs based models performance. (6) Effect of the change in grid orientation on the QM-MIFs-based models performance. (7) Activity cliff pairs determination. This material is available free of charge via the Internet at <http://pubs.acs.org>.

AUTHOR INFORMATION

Corresponding Author

*E-mail: Tim.Clark@chemie.uni-erlangen.de.

Notes

The authors declare no competing financial interest.

ACKNOWLEDGMENTS

This work was supported by the Bundesministerium für Bildung und Forschung (BMBF) as part of the hpCADD project ([www.hpcadd.com](http://hpcadd.com)), by Cepos InSilico GmbH, and by a grant of a Fellowship to A.E.K. from the Deutscher Akademischer Austauschdienst. Molecular graphics in the Introduction section were generated using MOLEKEL 4.3.^{106,107} Molecular graphics in the Results and Discussion section were generated using the UCSF Chimera package.¹⁰⁸ Chimera is developed by the Resource for Biocomputing, Visualization, and Informatics at the University of California, San Francisco, funded by grants from the National Institutes of Health National Center for Research Resources (2P41RR001081) and National Institute of General Medical Sciences (9P41GM103311).

REFERENCES

- (1) Van Drie, J. H. Pharmacophore discovery: Lessons learned. *Curr. Pharm. Des.* **2003**, *9* (20), 1649–1664.
- (2) Shim, J.; MacKerell, A. D. Computational ligand-based rational design: role of conformational sampling and force fields in model development. *Med. Chem. Comm.* **2011**, *2* (5), 356–370.
- (3) Richards, W. G. Computers in drug design. *Pure Appl. Chem.* **1993**, *65* (2), 231–234.
- (4) Cramer, R. D.; Patterson, D. E.; Bunce, J. D. Comparative molecular-field analysis (CoMFA). 1. effect of shape on binding of steroids to carrier proteins. *J. Am. Chem. Soc.* **1988**, *110* (18), 5959–5967.
- (5) Klebe, G.; Abraham, U.; Mietzner, T. Molecular similarity indexes in a comparative-analysis (CoMSIA) of drug molecules to correlate and predict their biological-activity. *J. Med. Chem.* **1994**, *37* (24), 4130–4146.
- (6) Klebe, G. Comparative molecular similarity indices analysis: CoMSIA. *Perspect. Drug Discovery Des.* **1998**, *12*, 87–104.
- (7) Verma, J.; Khedkar, V. M.; Coutinho, E. C. 3D-QSAR in drug design: A review. *Curr. Top. Med. Chem.* **2010**, *10*, 95–115.
- (8) Cramer, R. D.; Wendt, B. Pushing the boundaries of 3D-QSAR. *J. Comput.-Aided Mol. Des.* **2007**, *21* (1–3), 23–32.
- (9) Wold, S.; Albano, C.; Dunn, W. J.; Edlund, U.; Esbenson, K.; Geladi, P.; Hellberg, S.; Lindberg, W.; Sjöström, M. Multivariate Data Analysis in Chemistry. In *Chemometrics: Mathematics and Statistics in Chemistry*; Kowalski, B. R., Ed.; D. Reidel Publishing Company: The Netherlands, 1984; pp 17–95.
- (10) Dunn, W. J.; Wold, S.; Edlund, U.; Hellberg, S.; Gasteiger, J. Multivariate structure–activity relationships between data from a battery of biological tests and an ensemble of structure descriptors: The PLS method. *Quant. Struct.-Act. Relat.* **1984**, *3* (4), 131–137.
- (11) Geladi, P. Notes on the history and nature of partial least squares (PLS) modelling. *J. Chemom.* **1988**, *2* (4), 231–246.
- (12) Kubinyi, H., Comparative Molecular Field Analysis (CoMFA). In *Encyclopedia of Computational Chemistry*; Wiley: New York, 1998; Vol. 1, pp 448–460.
- (13) Kellogg, G. E.; Semus, S. F.; Abraham, D. J. Hint: A new method of empirical hydrophobic field calculation for CoMFA. *J. Comput.-Aided Mol. Des.* **1991**, *5* (6), 545–552.

- (14) Klebe, G.; Abraham, U. Comparative molecular similarity index Analysis (CoMSIA) to study hydrogen-bonding properties and to score combinatorial libraries. *J. Comput.-Aided Mol. Des.* **1999**, *13* (1), 1–10.
- (15) Böhm, M.; Klebe, G. Development of new hydrogen-bond descriptors and their application to comparative molecular field analyses. *J. Med. Chem.* **2002**, *45* (8), 1585–1597.
- (16) Wireko, F. C.; Kellogg, G. E.; Abraham, D. J. Allosteric modifiers of hemoglobin. 2. Crystallographically determined binding-sites and hydrophobic binding interaction analysis of novel hemoglobin oxygen effectors. *J. Med. Chem.* **1991**, *34* (2), 758–767.
- (17) Abraham, D. J.; Kellogg, G. E. The effect of physical organic properties on hydrophobic fields. *J. Comput.-Aided Mol. Des.* **1994**, *8* (1), 41–9.
- (18) Goodford, P. Multivariate characterization of molecules for QSAR analysis. *J. Chemom.* **1996**, *10* (2), 107–117.
- (19) Gaillard, P.; Carrupt, P. A.; Testa, B.; Boudon, A. Molecular lipophilicity potential, a tool in 3D QSAR: Method and applications. *J. Comput.-Aided Mol. Des.* **1994**, *8* (2), 83–96.
- (20) Paton, R. S.; Goodman, J. M. Hydrogen bonding and π -stacking: How reliable are force fields? A critical evaluation of force field descriptions of nonbonded interactions. *J. Chem. Inf. Model.* **2009**, *49* (4), 944–955.
- (21) Politzer, P.; Lane, P.; Concha, M. C.; Ma, Y.; Murray, J. S. An overview of halogen bonding. *J. Mol. Model.* **2007**, *13* (2), 305–311.
- (22) Politzer, P.; Murray, J. S.; Clark, T. Halogen bonding: An electrostatically-driven highly directional noncovalent interaction. *Phys. Chem. Chem. Phys.* **2010**, *12* (28), 7748–7757.
- (23) Murray, J. S.; Riley, K. E.; Politzer, P.; Clark, T. Directional weak intermolecular interactions: σ -Hole bonding. *Aust. J. Chem.* **2010**, *63* (12), 1598–1607.
- (24) Güssregen, S.; Matter, H.; Hessler, G.; Müller, M.; Schmidt, F.; Clark, T. 3D-QSAR based on quantum-chemical molecular fields: Toward an improved description of halogen interactions. *J. Chem. Inf. Model.* **2012**, *52* (9), 2441–2453.
- (25) Murray, J. S.; Lane, P.; Clark, T.; Riley, K. E.; Politzer, P. σ -Holes, π -holes and electrostatically-driven interactions. *J. Mol. Model.* **2012**, *18* (2), 541–548.
- (26) Clark, T. σ -Holes. *WIREs Comput. Mol. Sci.* **2013**, *3* (1), 13–20.
- (27) Rendine, S.; Pieraccini, S.; Forni, A.; Sironi, M. Halogen bonding in ligand-receptor systems in the framework of classical force fields. *Phys. Chem. Chem. Phys.* **2011**, *13* (43), 19508–19516.
- (28) Ibrahim, M. A. A. AMBER empirical potential describes the geometry and energy of noncovalent halogen interactions better than advanced semiempirical quantum mechanical method PM6-DH2X. *J. Phys. Chem. B* **2012**, *116* (11), 3659–3669.
- (29) Jorgensen, W. L.; Schyman, P. Treatment of halogen bonding in the OPLS-AA force field: Application to potent Anti-HIV agents. *J. Chem. Theory Comput.* **2012**, *8* (10), 3895–3901.
- (30) Kolar, M.; Hobza, P. On extension of the current biomolecular empirical force field for the description of halogen bonds. *J. Chem. Theory Comput.* **2012**, *8* (4), 1325–1333.
- (31) Ma, J. C.; Dougherty, D. A. The cation- π interaction. *Chem. Rev.* **1997**, *97* (5), 1303–1324.
- (32) Meyer, E. A.; Castellano, R. K.; Diederich, F. Interactions with aromatic rings in chemical and biological recognition. *Angew. Chem., Int. Ed.* **2003**, *42* (11), 1210–1250.
- (33) Zhou, T.; Huang, D. Z.; Cafilisch, A. Quantum mechanical methods for drug design. *Curr. Top. Med. Chem.* **2010**, *10* (1), 33–45.
- (34) Cavalli, A.; Carloni, P.; Recanatini, M. Target-related applications of first principles quantum chemical methods in drug design. *Chem. Rev.* **2006**, *106* (9), 3497–3519.
- (35) Peters, M. B.; Raha, K.; Merz, K. M. Quantum mechanics in structure-based drug design. *Curr. Opin. Drug Discovery Dev.* **2006**, *9* (3), 370–379.
- (36) Peters, M. B.; Merz, K. M. Semiempirical comparative binding energy analysis (SE-COMBINE) of a series of trypsin inhibitors. *J. Chem. Theory Comput.* **2006**, *2*, 383–399.
- (37) Raha, K.; Peters, M. B.; Wang, B.; Yu, N.; Wollacott, A. M.; Westerhoff, L. M.; Merz, K. M. The role of quantum mechanics in structure-based drug design. *Drug Discovery Today* **2007**, *12* (17–18), 725–731.
- (38) Yamagami, C.; Motohashi, N.; Akamatsu, M. Quantum chemical and 3-D-QSAR (CoMFA) studies of benzalacetones and 1,1,1-trifluoro-4-phenyl-3-buten-2-ones. *Bioorg. Med. Chem. Lett.* **2002**, *12* (17), 2281–2285.
- (39) Occhiato, E. G.; Ferrali, A.; Menchi, G.; Guarna, A.; Danza, G.; Comerci, A.; Mancina, R.; Serio, M.; Garotta, G.; Cavalli, A.; De Vivo, M.; Recanatini, M. Synthesis, biological activity, and three-dimensional quantitative structure-activity relationship model for a series of benzo[c]quinolizin-3-ones, nonsteroidal inhibitors of human steroid 5 α -reductase 1. *J. Med. Chem.* **2004**, *47* (14), 3546–3560.
- (40) Wan, J.; Zhang, L.; Yang, G. F. Quantitative structure-activity relationships for phenyl triazolinones of protoporphyrinogen oxidase inhibitors: A density functional theory study. *J. Comput. Chem.* **2004**, *25* (15), 1827–1832.
- (41) Wan, J.; Zhang, L.; Yang, G. F.; Zhan, C. G. Quantitative structure-activity relationship for cyclic imide derivatives of protoporphyrinogen oxidase inhibitors: A study of quantum chemical descriptors from density functional theory. *J. Chem. Inf. Comput. Sci.* **2004**, *44* (6), 2099–2105.
- (42) Lepp, Z.; Chuman, H. Connecting traditional QSAR and molecular simulations of papain hydrolysis - importance of charge transfer. *Bioorg. Med. Chem.* **2005**, *13* (9), 3093–3105.
- (43) Singh, P. P.; Srivastava, H. K.; Pasha, F. A. DFT-based QSAR study of testosterone and its derivatives. *Bioorg. Med. Chem.* **2004**, *12* (1), 171–177.
- (44) Pasha, F. A.; Muddassar, M.; Jung, H.; Yang, B. S.; Lee, C. J.; Oh, J. S.; Cho, S. J.; Cho, H. QM and pharmacophore based 3D-QSAR of MK886 analogues against mPGES-1. *Bull. Korean Chem. Soc.* **2008**, *29* (3), 647–655.
- (45) Beck, M. E.; Schindler, M. Quantitative structure-activity relations based on quantum theory and wavelet transformations. *Chem. Phys.* **2009**, *356* (1–3), 121–130.
- (46) Van Damme, S.; Bultinck, P. Conceptual DFT properties-based 3D QSAR: Analysis of inhibitors of the nicotine metabolizing CYP2A6 enzyme. *J. Comput. Chem.* **2009**, *30* (12), 1749–1757.
- (47) Dolezal, R.; Van Damme, S.; Bultinck, P.; Waisser, K. QSAR analysis of salicylamide isosteres with the use of quantum chemical molecular descriptors. *Eur. J. Med. Chem.* **2009**, *44* (2), 869–876.
- (48) Van Damme, S.; Bultinck, P. 3D QSAR based on conceptual DFT molecular fields: Antituberculous activity. *J. Mol. Struct. THEOCHEM* **2010**, *943* (1–3), 83–89.
- (49) Klamt, A.; Thormann, M.; Wichmann, K.; Tosco, P. COSMOsar3D: Molecular field analysis based on local COSMO sigma-profiles. *J. Chem. Inf. Model.* **2012**, *52* (8), 2157–2164.
- (50) Dixon, S.; Merz, K. M.; Lauri, G.; Ianni, J. C. QM-QSAR: Utilization of a semiempirical probe potential in a field-based QSAR method. *J. Comput. Chem.* **2005**, *26* (1), 23–34.
- (51) Clark, T.; Stewart, J. J. P. MNDO-Like Semiempirical Molecular Orbital Theory and Its Application to Large Systems. In *Computational Methods for Large Systems: Electronic Structure Approaches for Biotechnology and Nanotechnology*, 1st ed.; Reimers, J. R., Ed.; John Wiley & Sons, Inc.: Hoboken, NJ, 2010; pp 259–286.
- (52) Purvis, G. D., III On the use of isovalued surfaces to determine molecule shape and reaction pathways. *J. Comput.-Aided Mol. Des.* **1991**, *5* (1), 55–80.
- (53) Clark, T. QSAR and QSPR based solely on surface properties? *J. Mol. Graphics Modell.* **2004**, *22* (6), 519–525.
- (54) Dewar, M. J. S.; Zoebisch, E. G.; Healy, E. F.; Stewart, J. J. P. AM1: A new general purpose quantum mechanical molecular model. *J. Am. Chem. Soc.* **1985**, *107* (13), 3902–3909.
- (55) Holder, A. AM1. In *Encyclopedia of Computational Chemistry*; Schleyer, P. v. R.; Allinger, N. L.; Clark, T., Gasteiger, J., Kollman, P. A., Schaefer, H. F. I., Schreiner, P. R., Eds.; John Wiley & Sons Ltd.: Chichester, U.K., 1998; Vol. 1, pp 8–11.
- (56) Nyburg, S. C. 'Polar Flattening': Non-spherical effective shapes of atoms in crystals. *Acta Crystallogr., Sect. A: Found. Crystallogr.* **1979**, *35* (Jul), 641–645.

- (57) Awwadi, F. F.; Willett, R. D.; Peterson, K. A.; Twamley, B. The nature of halogen...halogen synthons: Crystallographic and theoretical studies. *Chem.—Eur. J.* **2006**, *12* (35), 8952–8960.
- (58) El Kerdawy, A.; Wick, C. R.; Hennemann, M.; Clark, T. Predicting the sites and energies of noncovalent intermolecular interactions using local properties. *J. Chem. Inf. Model.* **2012**, *52* (4), 1061–1071.
- (59) Murray, J. S.; Politzer, P. Statistical analysis of the molecular surface electrostatic potential: an approach to describing noncovalent interactions in condensed phases. *J. Mol. Struct. THEOCHEM* **1998**, *425* (1–2), 107–114.
- (60) Murray, J. S.; Lane, P.; Brinck, T.; Paulsen, K.; Grice, M. E.; Politzer, P. Relationships of critical constants and boiling points to computed molecular-surface properties. *J. Phys. Chem.* **1993**, *97* (37), 9369–9373.
- (61) Sjöberg, P.; Murray, J. S.; Brinck, T.; Politzer, P. Average local ionization energies on the molecular-surfaces of aromatic systems as guides to chemical-reactivity. *Can. J. Chem.* **1990**, *68* (8), 1440–1443.
- (62) Politzer, P.; Murray, J. S.; Concha, M. C. The complementary roles of molecular surface electrostatic potentials and average local ionization energies with respect to electrophilic processes. *Int. J. Quantum Chem.* **2002**, *88* (1), 19–27.
- (63) Hussein, W.; Walker, C. G.; Peralta-Inga, Z.; Murray, J. S. Computed electrostatic potentials and average local ionization energies on the molecular surfaces of some tetracyclines. *Int. J. Quantum Chem.* **2001**, *82* (4), 160–169.
- (64) Murray, J. S.; Abu-Awwad, F.; Politzer, P. Characterization of aromatic hydrocarbons by means of average local ionization energies on their molecular surfaces. *J. Mol. Struct. THEOCHEM* **2000**, *501*, 241–250.
- (65) Ehresmann, B.; Martin, B.; Horn, A. H. C.; Clark, T. Local molecular properties and their use in predicting reactivity. *J. Mol. Model.* **2003**, *9* (5), 342–347.
- (66) Clark, T. The local electron affinity for non-minimal basis sets. *J. Mol. Model.* **2010**, *16* (7), 1231–1238.
- (67) Schurer, G.; Gedeck, P.; Gottschalk, M.; Clark, T. Accurate parametrized variational calculations of the molecular electronic polarizability by NDDO-based methods. *Int. J. Quantum Chem.* **1999**, *75* (1), 17–31.
- (68) Rinaldi, D.; Rivail, J. L. Molecular polarizability and dielectric effect of medium in liquid phase: Theoretical study of water molecule and its dimers. *Theor. Chim. Acta* **1973**, *32* (1), 57–70.
- (69) Rinaldi, D.; Rivail, J. L. Calculation of molecular electronic polarizabilities: Comparison of different methods. *Theor. Chim. Acta* **1974**, *32* (3), 243–251.
- (70) Martin, B.; Gedeck, P.; Clark, T. Additive NDDO-based atomic polarizability model. *Int. J. Quantum Chem.* **2000**, *77* (1), 473–497.
- (71) Böhm, H. J.; Klebe, G. What can we learn from molecular recognition in protein–ligand complexes for the design of new drugs? *Angew. Chem., Int. Ed.* **1996**, *35* (22), 2589–2614.
- (72) Bissantz, C.; Kuhn, B.; Stahl, M. A medicinal chemist's guide to molecular interactions. *J. Med. Chem.* **2010**, *53* (14), S061–S084.
- (73) Furet, P.; Sele, A.; Cohen, N. C. 3D molecular lipophilicity potential profiles: A new tool in molecular modeling. *J. Mol. Graphics* **1988**, *6* (4), 182–189.
- (74) Fauchere, J. L.; Quarendon, P.; Kaetterer, L. Estimating and representing hydrophobicity potential. *J. Mol. Graphics* **1988**, *6* (4), 203–206.
- (75) Audry, E.; Dubost, J. P.; Dallet, P.; Langlois, M. H.; Colleter, J. C. Application of molecular lipophilicity potential to a series of beta-adrenolytic amines. *Eur. J. Med. Chem.* **1989**, *24* (2), 155–161.
- (76) Testa, B.; Carrupt, P. A.; Gaillard, P.; Billois, F.; Weber, P. Lipophilicity in molecular modeling. *Pharm. Res.* **1996**, *13* (3), 335–343.
- (77) Muehlbacher, M.; El Kerdawy, A.; Kramer, C.; Hudson, B.; Clark, T. Conformation-dependent QSPR models: logP(OW). *J. Chem. Inf. Model.* **2011**, *51* (9), 2408–2416.
- (78) Sutherland, J. J.; O'Brien, L. A.; Weaver, D. F. A comparison of methods for modeling quantitative structure–activity relationship. *J. Med. Chem.* **2004**, *47* (22), S541–S554.
- (79) Matter, H.; Will, D. W.; Nazare, M.; Schreuder, H.; Laux, V.; Wehner, V. Structural requirements for factor Xa inhibition by 3-oxybenzamides with neutral P1 substituents: Combining X-ray crystallography, 3D-QSAR, and tailored scoring functions. *J. Med. Chem.* **2005**, *48* (9), 3290–3312.
- (80) Depriest, S. A.; Mayer, D.; Naylor, C. B.; Marshall, G. R. 3D-QSAR of angiotensin-converting enzyme and thermolysin inhibitors: A comparison of CoMFA models based on deduced and experimentally determined active-site geometries. *J. Am. Chem. Soc.* **1993**, *115* (13), 5372–5384.
- (81) Gohlke, H.; Klebe, G. DrugScore meets CoMFA: Adaptation of fields for molecular comparison (AFMoC) or how to tailor knowledge-based pair-potentials to a particular protein. *J. Med. Chem.* **2002**, *45* (19), 4153–4170.
- (82) Böhm, M.; Stürzebecher, J.; Klebe, G. Three-dimensional quantitative structure-activity relationship analyses using comparative molecular field analysis and comparative molecular similarity indices analysis to elucidate selectivity differences of inhibitors binding to trypsin, thrombin, and factor Xa. *J. Med. Chem.* **1999**, *42* (3), 458–477.
- (83) Ferguson, A. M.; Heritage, T.; Jonathon, P.; Pack, S. E.; Phillips, L.; Rogan, J.; Snaith, P. J. EVA: A new theoretically based molecular descriptor for use in QSAR/QSPR analysis. *J. Comput.-Aided Mol. Des.* **1997**, *11* (2), 143–152.
- (84) Ginn, C. M. R.; Turner, D. B.; Willett, P.; Ferguson, A. M.; Heritage, T. W. Similarity searching in files of three-dimensional chemical structures: Evaluation of the EVA descriptor and combination of rankings using data fusion. *J. Chem. Inf. Comput. Sci.* **1997**, *37* (1), 23–37.
- (85) Heritage, T. W.; Ferguson, A. M.; Turner, D. B.; Willett, P. EVA: A novel theoretical descriptor for QSAR studies. *Perspect. Drug Discovery Des.* **1998**, *9–11*, 381–398.
- (86) Turner, D. B.; Willett, P.; Ferguson, A. M.; Heritage, T. Evaluation of a novel infrared range vibration-based descriptor (EVA) for QSAR studies 0.1. General application. *J. Comput.-Aided Mol. Des.* **1997**, *11* (4), 409–422.
- (87) Heritage, T. W.; Lowis, D. R. Molecular Hologram QSAR. In *Rational Drug Design: Novel Methodology and Practical Applications*; Parrill, A. L., Reddy, M. R., Eds.; Oxford University Press: New York, 1999; pp 212–225.
- (88) McMartin, C.; Bohacek, R. S. QXP: Powerful, rapid computer algorithms for structure-based drug design. *J. Comput.-Aided Mol. Des.* **1997**, *11* (4), 333–344.
- (89) Weiner, S. J.; Kollman, P. A.; Case, D. A.; Singh, U. C.; Ghio, C.; Alagona, G.; Profeta, S.; Weiner, P.; New, A. Force-field for molecular mechanical simulation of nucleic-acids and proteins. *J. Am. Chem. Soc.* **1984**, *106* (3), 765–784.
- (90) Halgren, T. A. Maximally diagonal force-constants in dependent angle-bending coordinates. 2. Implications for the design of empirical force-fields. *J. Am. Chem. Soc.* **1990**, *112* (12), 4710–4723.
- (91) Clark, T.; Alex, A.; Beck, B.; Burckhardt, F.; Chandrasekhar, J.; Gedeck, P.; Horn, A.; Hutter, M.; Martin, B.; Rauhut, G.; Sauer, W.; Schindler, T.; Steinke, T. VAMP 10.0; Accelrys Inc.: San Diego, CA, U.S.A.; Erlangen, Germany, 2007.
- (92) Stewart, J. J. P. MOPAC6; Cepos InSilico Ltd.: Kempston, Bedford, U.K., 2009.
- (93) Hennemann, M.; Clark, T. EMPIRE; Universität Erlangen-Nürnberg and Cepos InSilico Ltd.: Kempston, Bedford, U.K., 2012. <http://www.ceposinsilico.de/products/empire.htm> (accessed May 29, 2013).
- (94) Clark, T.; Lin, J.; Horn, A. H. C. Parasurf 11; Universität Erlangen-Nürnberg and CEPOS InSilico Ltd.: Kempston, Bedford, U.K., 2011. <http://www.ceposinsilico.de/products/parasurf.htm> (accessed May 29, 2013).
- (95) SAR-caddle; Cepos InSilico Ltd.: Kempston, Bedford, U.K., 2012. <http://www.ceposinsilico.de/products/sar-caddle.htm> (accessed May 29, 2013).
- (96) Wold, S. Cross-validatory estimation of number of components in factor and principal components models. *Technometrics* **1978**, *20* (4), 397–405.
- (97) Diaconis, P.; Efron, B. Computer-intensive methods in statistics. *Sci. Am.* **1983**, *248* (5), 116–130.

- (98) Cramer, R. D.; Bunce, J. D.; Patterson, D. E.; Frank, I. E. Cross-validation, bootstrapping, and partial least-squares compared with multiple-regression in conventional QSAR studies. *Quant. Struct.-Act. Relat.* **1988**, *7* (1), 18–25.
- (99) Guha, R.; Van Drie, J. H. Structure–activity landscape index: Identifying and quantifying activity cliffs. *J. Chem. Inf. Model.* **2008**, *48* (3), 646–658.
- (100) Cho, S. J.; Tropsha, A. Cross-validated R^2 -guided region selection for comparative molecular field analysis: A simple method to achieve consistent results. *J. Med. Chem.* **1995**, *38* (7), 1060–1066.
- (101) Tropsha, A.; Cho, S. J. Cross-validated R^2 guided region selection for CoMFA studies. *Perspect. Drug Discovery Des.* **1998**, *12*, 57–69.
- (102) Matter, H.; Nazare, M.; Güssregen, S.; Will, D. W.; Schreuder, H.; Bauer, A.; Urmann, M.; Ritter, K.; Wagner, M.; Wehner, V. Evidence for C-Cl/C-Br... π interactions as an important contribution to protein–ligand binding affinity. *Angew. Chem., Int. Ed.* **2009**, *48* (16), 2911–2916.
- (103) Abel, R.; Young, T.; Farid, R.; Berne, B. J.; Friesner, R. A. Role of the active-site solvent in the thermodynamics of factor Xa ligand binding. *J. Am. Chem. Soc.* **2008**, *130* (9), 2817–2831.
- (104) Abel, R.; Salam, N. K.; Shelley, J.; Farid, R.; Friesner, R. A.; Sherman, W. Contribution of explicit solvent effects to the binding affinity of small-molecule inhibitors in blood coagulation factor serine proteases. *Chem. Med. Chem.* **2011**, *6* (6), 1049–1066.
- (105) Johnson, S. R. The trouble with QSAR (or how I learned to stop worrying and embrace fallacy). *J. Chem. Inf. Model.* **2008**, *48* (1), 25–26.
- (106) Flükiger, P.; Lüthi, H. P.; Portmann, S.; Weber, J. *MOLEKEL 4.3*; Swiss Center for Scientific Computing: Manno, Switzerland, 2000–2002.
- (107) Portmann, S.; Lüthi, H. P. *MOLEKEL*: An interactive molecular graphics tool. *Chimia* **2000**, *54* (12), 766–770.
- (108) Pettersen, E. F.; Goddard, T. D.; Huang, C. C.; Couch, G. S.; Greenblatt, D. M.; Meng, E. C.; Ferrin, T. E. UCSF chimera: A visualization system for exploratory research and analysis. *J. Comput. Chem.* **2004**, *25* (13), 1605–1612.